AAAS
Research
Volume 2022, Article ID 9870149, 10 pages
https://doi.org/10.34133/2022/9870149

Research
A SCIENCE PARTNER JOURNAL

Research Article

Continuity Scaling: A Rigorous Framework for Detecting and Quantifying Causality Accurately

Xiong Ying,[1,2,3] **Si-Yang Leng**,[2,4] **Huan-Fei Ma**,[5] **Qing Nie**,[6] **Ying-Cheng Lai**,[7]
and Wei Lin[1,2,3,8]

[1]*School of Mathematical Sciences, SCMS, and SCAM, Fudan University, Shanghai 200433, China*
[2]*Research Institute for Intelligent Complex Systems, CCSB, and LCNBI, Fudan University, Shanghai 200433, China*
[3]*State Key Laboratory of Medical Neurobiology and MOE Frontiers Center for Brain Science, Institutes of Brain Science, Fudan University, Shanghai 200032, China*
[4]*Institute of AI and Robotics, Academy for Engineering and Technology, Fudan University, Shanghai 200433, China*
[5]*School of Mathematical Sciences, Soochow University, Suzhou 215006, China*
[6]*Department of Mathematics, Department of Developmental and Cell Biology, And NSF-Simons Center for Multiscale Cell Fate Research, University of California, Irvine, CA 92697-3875, USA*
[7]*School of Electrical, Computer, And Energy Engineering, Arizona State University, Tempe, Arizona 85287-5706, USA*
[8]*Shanghai Artificial Intelligence Laboratory, Shanghai 200232, China*

Correspondence should be addressed to Wei Lin; wlin@fudan.edu.cn

Received 7 March 2022; Accepted 24 March 2022; Published 4 May 2022

Data-based detection and quantification of causation in complex, nonlinear dynamical systems is of paramount importance to science, engineering, and beyond. Inspired by the widely used methodology in recent years, the cross-map-based techniques, we develop a general framework to advance towards a comprehensive understanding of dynamical causal mechanisms, which is consistent with the natural interpretation of causality. In particular, instead of measuring the smoothness of the cross-map as conventionally implemented, we define causation through measuring the *scaling law* for the continuity of the investigated dynamical system directly. The uncovered scaling law enables accurate, reliable, and efficient detection of causation and assessment of its strength in general complex dynamical systems, outperforming those existing representative methods. The continuity scaling-based framework is rigorously established and demonstrated using datasets from model complex systems and the real world.

1. Introduction

Identifying and ascertaining causal relations are a problem of paramount importance to science and engineering with broad applications [1–3]. For example, accurate detection of causation is the key to identifying the origin of diseases in precision medicine [4] and is important to fields such as psychiatry [5]. Traditionally, associational concepts are often misinterpreted as causation [6, 7], while causal analysis in fact goes one step further beyond association in a sense that, instead of using static conditions, causation is induced under changing conditions [8]. The principle of Granger causality formalizes a paradigmatic framework [9–11], quantifying causality in terms of prediction improvements, but, because of its linear, multivariate, and statistical regression nature, the various derived methods require extensive data [12]. Entropy-based methods [13–20] face a similar difficulty. Another issue with the Granger causality is the fundamental requirement of separability of the underlying dynamical variables, which usually cannot be met in the real world systems. To overcome these difficulties, the cross-map-based techniques, paradigms tailored to dynamical systems, have been developed and have gained widespread attention in the past decade [21–36].

The cross-map is originated from nonlinear time series analysis [37–42]. A brief understanding of such a map is as follows. Consider two subsystems: X and Y. In the reconstructed phase space of X, if for any state vector at a time a set of neighboring vectors can be found, the set of the cross-mapped vectors, which are the partners with equal time of X, could be available in Y. The cross-map underlying the reconstructed spaces can be written as $Y_t = \Phi(X_t)$ (where X_t and Y_t are delay coordinates with sufficiently large dimensions) for the case of Y *unidirectionally* causing X while, mathematically, its inverse map does not exist [34]. In practice, using the prior knowledge on the true causality in toy models or/and the assumption on the expanding property of Φ (representing by its Jacobian's singular value larger than one in the topological causality framework [24]), scientists developed many practically useful techniques based on the cross-map for causality detection. For instance, the "activity" method, originally designed to measure the continuity of the inverse of the cross-map, compares the divergence of the cross-mapped vectors to the state vector in X with the divergence of the independently-selected neighboring vectors to the same state vector [22, 23]. The topological causality measures the divergence rate of the cross-mapped vectors from the state vectors in Y [24], and the convergent cross-mapping (CCM), increasing the length of time series, compares the true state vector Y with the average of the cross-mapped vectors, as the estimation of Y [21, 25–36]. Then, the change of the divergence or the accuracy of the estimation is statistically evaluated for determining the causation from Y to X. Inversely, the causation from X to Y can be evaluated in an analogous manner. The above evaluations [21, 24, 26–36] can be understood at a conceptional and qualitative level and perform well in many demonstrations.

In this work, striving for a comprehensive understanding of causal mechanisms and inspired by the cross-map-based techniques, we develop a mathematically rigorous framework for detecting causality in nonlinear dynamical systems, turning eyes towards investigating the original systems from their cross-maps, which is also logically consistent with the natural interpretation of causality as functional dependences [2, 8]. The skills used in cross-map-based methods are assimilated in our framework, while we directly study the original dynamical systems or the reconstructed systems instead of the cross-maps. The foundation of our framework is the *scaling law* for the changing relation of ε with δ arising from the continuity for the investigated system, henceforth the term "continuity scaling". In addition to providing a theory, we demonstrate, using synthetic and real-world data, that our continuity scaling framework is accurate, computationally efficient, widely applicable, showing advantages over the existing methods.

2. Continuity Scaling Framework

To explain the mathematical idea behind the development of our framework, we use the following class of discrete time dynamical systems: $\mathbf{x}_{t+1} = \mathbf{f}(\mathbf{x}_t, \mathbf{y}_t)$ and $\mathbf{y}_{t+1} = \mathbf{g}(\mathbf{x}_t, \mathbf{y}_t)$ for $t \in \mathbb{N}$, where the state variables $\{\mathbf{x}_t\}_{t\in\mathbb{N}}$, $\{\mathbf{y}_t\}_{t\in\mathbb{N}}$ evolve in the compact manifolds $\mathscr{M}$, $\mathscr{N}$ of dimension $D_{\mathscr{M}}$, $D_{\mathscr{N}}$ under sufficiently smooth map $\mathbf{f}$, $\mathbf{g}$, respectively. We adopt the common recognition of causality in dynamical systems.

Definition 1. If the dependence of $\mathbf{f}(\mathbf{x}, \mathbf{y})$ on $\mathbf{y}$ is nontrivial (i.e., a directional coupling exists), a variation in $\mathbf{y}$ results in a change in the value of $\mathbf{f}(\mathbf{x}, \mathbf{y})$ for any given $\mathbf{x}$, which, according to the natural interpretation of causality [2, 43], admits that $\mathbf{y} : \{\mathbf{y}_t\}_{t\in\mathbb{N}}$ has a direct causal effect on $\mathbf{x} : \{\mathbf{x}_t\}_{t\in\mathbb{N}}$, denoted by $\mathbf{y} \hookrightarrow \mathbf{x}$, as shown in the upper panel of Figure 1(a).

We now interpret the causal relationship stipulated by the continuity of a function. Let $\mathbf{f}_{\mathbf{x}_{\mathrm{g}}}(\cdot) \triangleq \mathbf{f}(\mathbf{x}_{\mathrm{g}}, \cdot)$ for a given point $\mathbf{x}_{\mathrm{g}} \in \mathscr{M}$. For any $\mathbf{y}_{\mathrm{P}} \in \mathscr{N}$, we denote its image under the given function by $\mathbf{x}_{\mathrm{I}} \triangleq \mathbf{f}_{\mathbf{x}_{\mathrm{g}}}(\mathbf{y}_{\mathrm{P}})$. Applying the logic statement of a continuous function to $\mathbf{f}_{\mathbf{x}_{\mathrm{g}}}(\cdot)$, we have that, for any neighborhood $\mathscr{O}(\mathbf{x}_{\mathrm{I}}, \varepsilon)$ centered at $\mathbf{x}_{\mathrm{I}}$ and of radius $\varepsilon > 0$, there exists a neighborhood $\mathscr{O}(\mathbf{y}_{\mathrm{P}}, \delta)$ centered at $\mathbf{y}_{\mathrm{P}}$ of radius $\delta > 0$, such that $\mathbf{f}_{\mathbf{x}_{\mathrm{g}}}(\mathscr{O}(\mathbf{y}_{\mathrm{P}}, \delta)) \subset \mathscr{O}(\mathbf{x}_{\mathrm{I}}, \varepsilon)$. The neighborhood and its radius are defined by

$$\mathscr{O}(\mathbf{p}, h) = \{\mathbf{s} \in \mathscr{S} | \mathrm{dist}_{\mathscr{S}}(\mathbf{s}, \mathbf{p}) < h\}, \mathbf{p} \in \mathscr{S}, h > 0, \tag{1}$$

where $\mathrm{dist}_{\mathscr{S}}(\cdot, \cdot)$ represents an appropriate metric describing the distance between two given points in a specified manifold $\mathscr{S}$ with $\mathscr{S} = \mathscr{M}$ or $\mathscr{N}$. The meaning of this mathematical statement is that, if we have a neighborhood of the resulting variable $\mathbf{x}_I$ first, we can then find a neighborhood for the causal variable $\mathbf{y}_P$ to satisfy the above mapping and inclusion relation. This operation of "first-ε-then-δ" provides a rigorous base for the principle that the information about the resulting variable can be used to estimate the information of the causal variable and therefore to ascertain causation, as indicated by the long arrow in the middle panels of Figure 1(a). Note that, the existence of the $\delta > 0$ neighborhood is always guaranteed for a continuous map $\mathbf{f}_{\mathbf{x}_{\mathrm{g}}}$. In fact, due to the compactness of the manifold $\mathscr{N}$, a largest value of δ exists. However, if $\mathbf{y}_P$ does not have an explicit causal effect on the variable $\mathbf{x}_I$, i.e., $\mathbf{f}_{\mathbf{x}_{\mathrm{g}}}$ is independent of $\mathbf{y}_P$, the existence of δ is still assured but it is independent of the value of ε, as shown in the upper panel of Figure 1(b). This means that merely determining the existence of a δ-neighborhood is not enough for inferring causation - it is necessary to vary ε systematically and to examine the scaling relation between δ and ε. In the following we discuss a number of scenarios.

Case I. Dynamical variables $\{(\mathbf{x}_t, \mathbf{y}_t)\}_{t\in\mathbb{N}}$ are fully measurable. For any given constant $\varepsilon_{\mathbf{x}} > 0$, the set $\{\mathbf{x}_\tau \in \mathscr{M} | \tau \in I^t_{\mathbf{x}}(\varepsilon_{\mathbf{x}})\}$ can be used to approximate the neighborhood $\mathscr{O}(\mathbf{x}_{t+1}, \varepsilon_{\mathbf{x}})$, where the time index set is

$$I^t_{\mathbf{x}}(\varepsilon_{\mathbf{x}}) \triangleq \{\tau \in \mathbb{N} | \mathrm{dist}_{\mathscr{M}}(\mathbf{x}_{t+1}, \mathbf{x}_\tau) < \varepsilon_{\mathbf{x}}\}. \tag{2}$$

The radius $\delta^t_{\mathbf{y}} = \delta^t_{\mathbf{y}}(\varepsilon_{\mathbf{x}})$ of the neighborhood $\mathscr{O}(\mathbf{y}_t, \delta^t_{\mathbf{y}})$

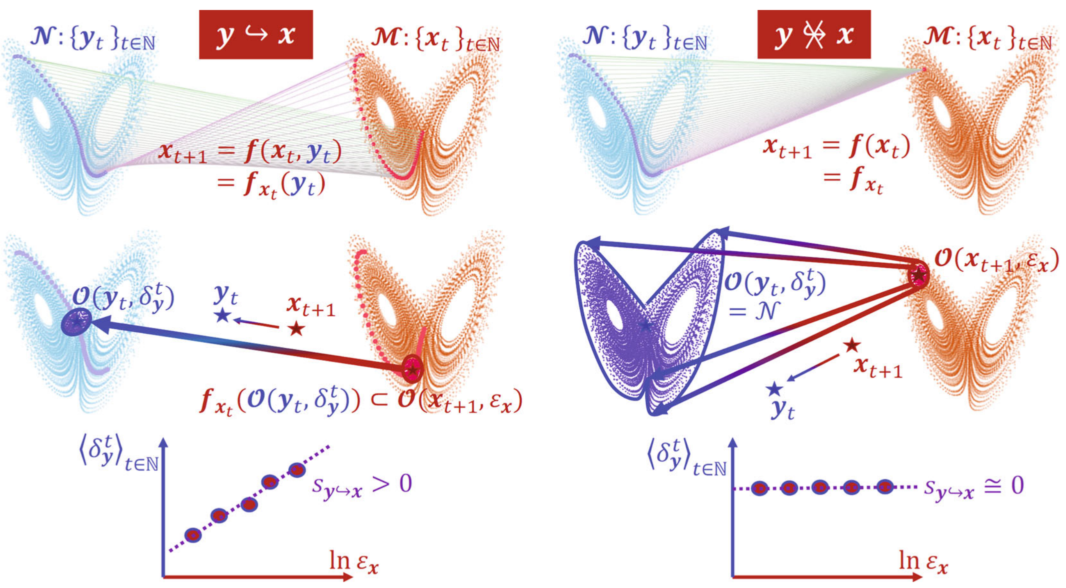

(a)

(b)

Figure 1: Illustration of causal relation between two sets of dynamical variables. (a) Existence of causation from $\mathbf{y}$ in $\mathcal{N}$ to $\mathbf{x}$ in $\mathcal{M}$, where each correspondence from $\mathbf{x}_{t+1}$ to $\mathbf{y}_t$ is one-to-one, represented by the line or the arrow, respectively, in the upper and the middle panels. In this case, a change in $\ln \varepsilon_{\mathbf{x}}$ results in a direct change in $\delta_{\mathbf{y}}$ (the lower panel) with $\varepsilon_{\mathbf{x}}$ and $\delta_{\mathbf{y}}$ denoting the neighborhood size of the resulting variable $\mathbf{x}$ and of the causal variable $\mathbf{y}$, respectively. (b) Absence of causation from $\mathbf{y}$ to $\mathbf{x}$, where every point on each trajectory, $\{\mathbf{y}_t\}$, in $\mathcal{N}$ could be the correspondent point from $\mathbf{x}_{t+1}$ in $\mathcal{M}$ (the upper panel) and thus every point in $\mathcal{N}$ belongs to the largest δ-neighborhood of $\mathbf{y}_t$ (the middle panel). In this case, $\delta_{\mathbf{y}}$ does not depend on $\varepsilon_{\mathbf{x}}$ (the lower panel). Also refer to the supplemental animation for illustration.

satisfying $\mathbf{f}_{\mathbf{x}_g=\mathbf{x}_t}(\mathcal{O}(\mathbf{y}_t, \delta_{\mathbf{y}}^t)) \subset \mathcal{O}(\mathbf{x}_{t+1}, \varepsilon_{\mathbf{x}})$ can be estimated as

$$\delta_{\mathbf{y}}^t(\varepsilon_{\mathbf{x}}) \triangleq \left\{\#\left[\bar{I}_{\mathbf{x}}^t(\varepsilon_{\mathbf{x}})\right]\right\}^{-1} \sum_{\tau\in\bar{I}_{\mathbf{x}}^t(\varepsilon_{\mathbf{x}})} \mathrm{dist}_{\mathcal{N}}(\mathbf{y}_t, \mathbf{y}_{\tau-1}), \tag{3}$$

where $\#[\cdot]$ is the cardinality of the given set and the index set is $\bar{I}_{\mathbf{x}}^t(\varepsilon_{\mathbf{x}}) \triangleq \{\tau \in I_{\mathbf{x}}^t(\varepsilon_{\mathbf{x}}) | \mathrm{dist}_{\mathcal{M}}(\mathbf{x}_t, \mathbf{x}_{\tau-1}) < \varepsilon_{\mathbf{x}}\}$.

The strict mathematical steps for estimating $\delta_{\mathbf{y}}^t$ are given in Section II of Supplementary Information (SI). We emphasize that here correspondence between $\mathbf{x}_{t+1}$ and $\mathbf{y}_t$ is investigated, differing from the cross-map-based methods, with one-step time difference naturally arising. This consideration yields a key condition [DD], which is only need when considering the original iteration/flow and whose detailed description and universality are demonstrated in SI. We reveal a linear scaling law between $\langle \delta_{\mathbf{y}}^t \rangle_{t\in\mathbb{N}}$ and $\ln \varepsilon_{\mathbf{x}}$, as shown in the lower panels of Figure 1, whose slope $s_{\mathbf{y}\hookrightarrow\mathbf{x}}$ is an indicator of the correspondent relation between ε and δ and hence the causal relation $\mathbf{y}\hookrightarrow\mathbf{x}$. Here, $\langle\cdot\rangle_{t\in\mathbb{N}}$ denotes the average over time. In particular, a larger slope value implies a stronger causation in the direction from $\mathbf{y}$ to $\mathbf{x}$ as represented by the map functions $\mathbf{f}(\mathbf{x}_t, \mathbf{y}_t)$ (Figure 1(a)), while a near zero slope indicates null causation in this direction (Figure 1(b)). Likewise, possible causation in the reversed direction, $\mathbf{x}\hookrightarrow\mathbf{y}$, as represented by the function $\mathbf{g}(\mathbf{x}_t, \mathbf{y}_t)$, can be assessed analogously. And the unidirectional case when $\mathbf{f}(\mathbf{x}, \mathbf{y}) = \mathbf{f}_0(\mathbf{x})$ independent of $\mathbf{y}$ is uniformly considered in Case II. We summarize the consideration below and an argument for the generic existence of the scaling law is provided in Section II of SI.

Theorem 2. *For dynamical variables $\{(\mathbf{x}_t, \mathbf{y}_t)\}_{t\in\mathbb{N}}$ measured directly from the dynamical systems, if the slope $s_{\mathbf{y}\hookrightarrow\mathbf{x}}$ defined above is zero, no causation exists from $\mathbf{y}$ to $\mathbf{x}$. Otherwise, a directional coupling can be confirmed from $\mathbf{y}$ to $\mathbf{x}$ and the slope $s_{\mathbf{y}\hookrightarrow\mathbf{x}}$ increases monotonically with the coupling strength.*

Case II. The dynamical variables $\{(\mathbf{x}_t, \mathbf{y}_t)\}_{t\in\mathbb{N}}$ are not directly accessible but measurable time series $\{u_t\}_{t\in\mathbb{N}}$ and $\{v_t\}_{t\in\mathbb{N}}$ are available, where $u_t = u(\mathbf{x}_t)$ and $v_t = v(\mathbf{y}_t)$ with $u: \mathcal{M} \longrightarrow \mathbb{R}^{r_u}$ and $v: \mathcal{N} \longrightarrow \mathbb{R}^{r_v}$ being smooth observational functions. To assess causation from $\mathbf{y}$ to $\mathbf{x}$, we assume one-dimensional observational time series (for simplicity): $r_u = r_v = 1$, and use the classical delay-coordinate embedding method [37–42, 44] to reconstruct the phase space: $\mathbf{u}_t = (u_t, u_{t+\tau_u}, \cdots, u_{t+(d_u-1)\tau_u})^T$ and $\mathbf{v}_t = (v_t, v_{t+\tau_v}, \cdots, v_{t+(d_v-1)\tau_v})^T$, where $\tau_{u,v}$ is the delay time and $d_{u,v} > 2(D_{\mathcal{M}} + D_{\mathcal{N}})$ is the embedding dimension that can be determined using some standard criteria [45]. As illustrated in Figure 2, the dynamical evolution of the reconstructed states $\{(\mathbf{u}_t, \mathbf{v}_t)\}_{t\in\mathbb{N}}$ is governed by

$$\mathbf{u}_{t+1} = \tilde{\mathbf{f}}(\mathbf{u}_t, \mathbf{v}_t), \mathbf{v}_{t+1} = \tilde{\mathbf{g}}(\mathbf{u}_t, \mathbf{v}_t). \tag{4}$$

The map functions can be calculated as $\tilde{\mathbf{f}}(\mathbf{u}, \mathbf{v}) \triangleq \mathbf{E}_u \circ [\mathbf{f}, \mathbf{g}](\mathbf{\Pi}_1 \circ \mathbf{E}_u^{-1}(\mathbf{u}), \mathbf{\Pi}_2 \circ \mathbf{E}_v^{-1}(\mathbf{v}))$, $\tilde{\mathbf{g}}(\mathbf{u}, \mathbf{v}) \triangleq \mathbf{E}_v \circ [\mathbf{f}, \mathbf{g}](\mathbf{\Pi}_1 \circ \mathbf{E}_u^{-1}(\mathbf{u}), \mathbf{\Pi}_2 \circ \mathbf{E}_v^{-1}(\mathbf{v}))$, where the embedding (diffeomorphism)

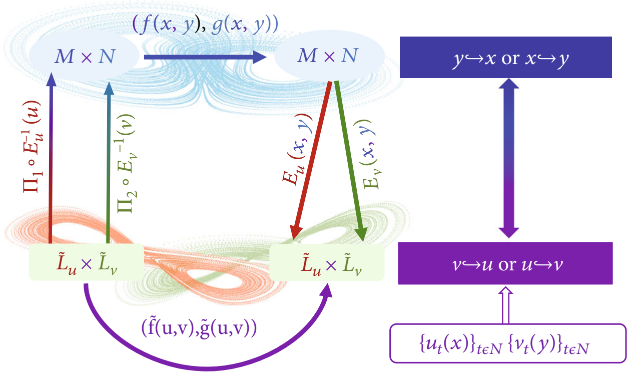

Figure 2: Illustration of system dynamics before and after embedding for Case II. In the left panel, the arrows describe how the original systems $(\mathbf{f}, \mathbf{g})$ is equivalent to the system $(\tilde{\mathbf{f}}, \tilde{\mathbf{g}})$ after embedding. In the right panel, causation between the internal variables $\mathbf{x}$ and $\mathbf{y}$ can be ascertained by detecting the causation between the variables $\mathbf{u}$ and $\mathbf{v}$ reconstructed from measured time series.

$\mathbf{E}_s$: $\mathscr{M} \times \mathscr{N} \longrightarrow \tilde{\mathscr{L}}_s \subset \mathbb{R}^{d_s}$ with $\tilde{\mathscr{L}}_s \triangleq \mathbf{E}_s(\mathscr{M} \times \mathscr{N})$, $s = u$ or v, is given by

$$\begin{aligned} \mathbf{E}_u(\mathbf{x},\mathbf{y}) &\triangleq (u(\mathbf{x}), u \circ \mathbf{\Pi}_1 \circ [\mathbf{f},\mathbf{g}]^{\tau_u}(\mathbf{x},\mathbf{y}), u \circ \mathbf{\Pi}_1 \circ \\ &\quad [\mathbf{f},\mathbf{g}]^{2\tau_u}(\mathbf{x},\mathbf{y}), \cdots, u \circ \mathbf{\Pi}_1 \circ [\mathbf{f},\mathbf{g}]^{(d_u-1)\tau_u}(\mathbf{x},\mathbf{y})), \\ \mathbf{E}_v(\mathbf{x},\mathbf{y}) &\triangleq (v(\mathbf{y}), v \circ \mathbf{\Pi}_2 \circ [\mathbf{f},\mathbf{g}]^{\tau_v}(\mathbf{x},\mathbf{y}), v \circ \mathbf{\Pi}_2 \circ \\ &\quad [\mathbf{f},\mathbf{g}]^{2\tau_v}(\mathbf{x},\mathbf{y}), \cdots, v \circ \mathbf{\Pi}_2 \circ [\mathbf{f},\mathbf{g}]^{(d_v-1)\tau_v}(\mathbf{x},\mathbf{y})), \end{aligned} \tag{5}$$

with the inverse function $\mathbf{E}_s^{-1}$ defined on $\tilde{\mathscr{L}}_s$, $[\mathbf{f},\mathbf{g}]^k$ representing the kth iteration of the map and the projection mappings as $\mathbf{\Pi}_1(\mathbf{x},\mathbf{y}) = \mathbf{x}$ and $\mathbf{\Pi}_2(\mathbf{x},\mathbf{y}) = \mathbf{y}$. Case II has now been reduced to Case I, and our continuity scaling framework can be used to ascertain the causation from $\mathbf{v}$ to $\mathbf{u}$ based on the measured time series with the indices $I_{\mathbf{u}}^t(\varepsilon_{\mathbf{u}})$, $\delta_{\mathbf{v}}^t(\varepsilon_{\mathbf{u}})$ and $s_{\mathbf{v}\hookrightarrow\mathbf{u}}$ (equations (2) and (3)).

Does the causation from $\mathbf{v}$ to $\mathbf{u}$ imply causation from $\mathbf{y}$ to $\mathbf{x}$? The answer is affirmative, which can be argued, as follows. If the original map function $\mathbf{f}$ is independent of $\mathbf{y}$: $\mathbf{f}(\mathbf{x},\mathbf{y}) = \mathbf{f}_0(\mathbf{x})$, there is no causation from $\mathbf{y}$ to $\mathbf{x}$. In this case, the embedding $\mathbf{E}_u(\mathbf{x},\mathbf{y})$ becomes independent of $\mathbf{y}$, degenerating into the form of $\mathbf{E}_u(\mathbf{x},\mathbf{y}) = \mathbf{E}_{u0}(\mathbf{x})$, a diffeomorphism from $\mathscr{M}$ to $\tilde{\mathscr{L}}_{u0} = \mathbf{E}_{u0}(\mathscr{M})$ only. As a result, equation (4) becomes $\mathbf{u}_{t+1} = \tilde{\mathbf{f}}_0(\mathbf{u}_t)$ and $\mathbf{v}_{t+1} = \tilde{\mathbf{g}}(\mathbf{u}_t, \mathbf{v}_t)$, where $\tilde{\mathbf{f}}_0(\mathbf{u}) = \mathbf{E}_{u0} \circ \mathbf{f} \circ \mathbf{E}_{u0}^{-1}(\mathbf{u})$ and the resulting mapping $\tilde{\mathbf{f}}_0$ is independent of $\mathbf{v}$. The independence can be validated by computing the slope $s_{\mathbf{v}\hookrightarrow\mathbf{u}}$ associated with the scaling relation between $\langle \delta_{\mathbf{v}}^t \rangle_{t\in\mathbb{N}}$ and $\ln \varepsilon_{\mathbf{u}}$, where a zero slope indicates null causation from $\mathbf{v}$ to $\mathbf{u}$ and hence null causation from $\mathbf{y}$ to $\mathbf{x}$. Conversely, a finite slope signifies causation between the variables. Thus, any type of causal relation (unidirectional or bi-directional) detected between the reconstructed state variables $\{(\mathbf{u}_t, \mathbf{v}_t)\}_{t\in\mathbb{N}}$ implies the same type of causal relation between the internal but inaccessible variables $\mathbf{x}$ and $\mathbf{y}$ of the original system.

Case III. The structure of the internal variables is completely unknown. Given the observational functions $\tilde{u}, \tilde{v}$: $\mathscr{M} \times \mathscr{N} \longrightarrow \mathbb{R}$ with $\tilde{u}_t = \tilde{u}(\mathbf{x}_t, \mathbf{y}_t)$ and $\tilde{v}_t = \tilde{v}(\mathbf{x}_t, \mathbf{y}_t)$, we first reconstruct the state space: $\tilde{\mathbf{u}}_t = (\tilde{u}_t, \tilde{u}_{t+\tau}, \cdots, \tilde{u}_{t+(d-1)\tau})^T$ and $\tilde{\mathbf{v}}_t = (\tilde{v}_t, \tilde{v}_{t+\tau}, \cdots, \tilde{v}_{t+(d-1)\tau})^T$. To detect and quantify causation from $\tilde{\mathbf{v}}$ to $\tilde{\mathbf{u}}$ (or vice versa), we carry out a continuity scaling analysis with the modified indices $I_{\tilde{\mathbf{u}}}^t(\varepsilon_{\tilde{\mathbf{u}}})$, $\delta_{\tilde{\mathbf{v}}}^t(\varepsilon_{\tilde{\mathbf{u}}})$ and $s_{\tilde{\mathbf{v}}\hookrightarrow\tilde{\mathbf{u}}}$. Differing from Case II, here, due to the lack of knowledge about the correspondence structure between the internal and observational variables, a causal relation for the latter does not definitely imply the same for the former.

Case IV. Continuous-time dynamical systems possessing a sufficiently smooth flow $\{\mathbf{S}_t\,; t \in \mathbb{R}\}$ on a compact manifold $\mathscr{H}$: $\mathrm{d}\mathbf{S}_t(\mathbf{u}_0)/dt = \chi(\mathbf{S}_t(\mathbf{u}_0))$, where χ is the vector field. Let $\{\hat{u}_{t=\omega n+v}\}_{n\in\mathbb{Z}}$ and $\{\hat{v}_{t=\omega n+v}\}_{n\in\mathbb{Z}}$ be two respective time series from the smooth observational functions $\hat{u}, \hat{v}$: $\mathscr{H} \longrightarrow \mathbb{R}$ with $\hat{u}_t = \hat{u}(\mathbf{S}_t)$ and $\hat{v}_t = \hat{v}(\mathbf{S}_t)$, where $1/\omega$ is the sampling rate and v is the time shift. Defining $\Xi \triangleq \mathbf{S}_\omega$: $\mathscr{H} \longrightarrow \mathscr{H}$ and $\hat{\mathbf{S}}_n \triangleq \mathbf{S}_{\omega n+v}(\mathbf{u}_0)$, we obtain a discrete-time system as $\hat{\mathbf{S}}_{n+1} = \Xi(\hat{\mathbf{S}}_n)$ with the observational functions as $\hat{u}_n = \hat{u}(\hat{\mathbf{S}}_n)$ and $\hat{v}_n = \hat{v}(\hat{\mathbf{S}}_n)$, reducing the case to Case III and rendering applicable our continuity scaling analysis to unveil and quantify the causal relation between $\{\hat{u}_{t=\omega n+v}\}_{n\in\mathbb{Z}}$ and $\{\hat{v}_{t=\omega n+v}\}_{n\in\mathbb{Z}}$. If the domains of $\hat{u}$ and $\hat{v}$ have their own restrictions on some particular subspaces, e.g., $\hat{u}$: $\mathscr{H}_u \longrightarrow \mathbb{R}$ and $\hat{v}$: $\mathscr{H}_v \longrightarrow \mathbb{R}$ with $\mathscr{H} = \mathscr{H}_u \oplus \mathscr{H}_v$, the case is further reduced to Case II, so the detected causal relation between the observational variables imply causation between the internal variables belonging to their respective subspaces.

3. Demonstrations: From Complex Dynamical Models to Real-World Networks

To demonstrate the efficacy of our continuity scaling framework and its superior performance, we have carried out extensive numerical tests with a large number of synthetic and empirical datasets, including those from gene regulatory networks as well as those of air pollution and hospital admission. The practical steps of the continuity scaling framework together with the significance test procedures are described in Methods. We present three representative examples here, while leaving others of significance to SI.

The first example is an ecological model of two unidirectionally interacting species: $x_{1,t+1} = x_{1,t}(3.8 - 3.8x_{1,t} - \mu_{12} x_{2,t})$ and $x_{2,t+1} = x_{2,t}(3.7 - 3.7x_{2,t} - \mu_{21}x_{1,t})$. With time series $\{(x_{1,t}, x_{2,t})\}_{t\in\mathbb{N}}$ obtained from different values of the coupling parameters, our continuity scaling framework yields correct results of different degree of unidirectional causation, as shown in Figures 3(a) and 3(b). In all cases, there exists a reasonable range of $\ln \varepsilon_{x_2}$ (neither too small nor too large) from which the slope $s_{x_1\hookrightarrow x_2}$ of the linear scaling can be extracted. The statistical significance of the estimated slope values and consequently the strength of causation can be assessed with the standard p-value test [46] (Methods and SI). An ecological model with bidirectional coupling has also been tested (see Section III of SI). Figures 3(c) and 3(d)

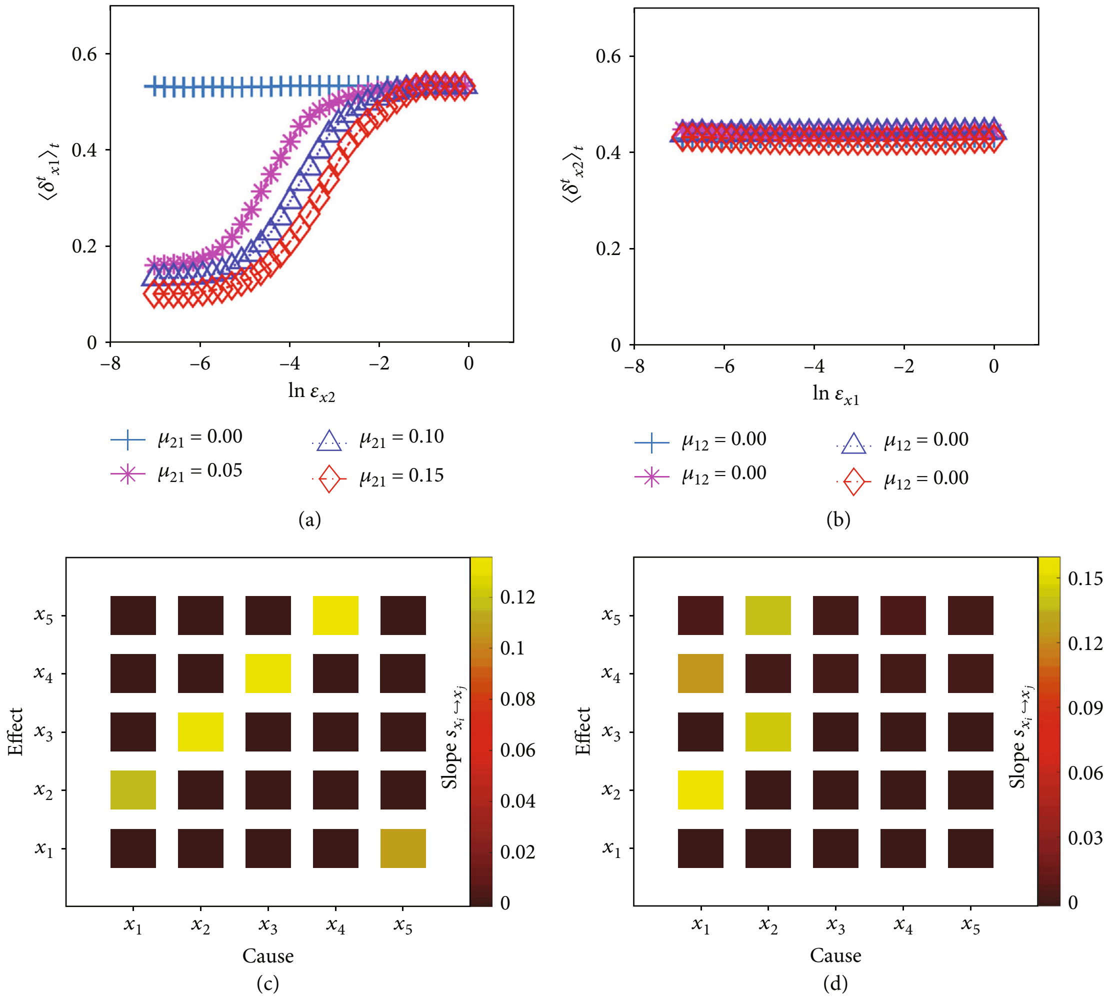

FIGURE 3: Ascertaining and characterizing causation in various ecological systems of interacting species. (a, b) Unidirectional causation of two coupled species. In (a), the values of the slope $s_{x_1 \hookrightarrow x_2}$ associated with the causal relation $x_1 \hookrightarrow x_2$ are approximately 0.0004, 0.1167, 0.1203, and 0.1238 for four different values of the coupling parameter μ_{21}. (b) Near zero slope values $s_{x_2 \hookrightarrow x_1}$ for $x_2 \hookrightarrow x_1$, indicating its nonexistence. (c, d) Inferred causal network of five species whose interacting structure is, respectively, that of a ring: $x_i \hookrightarrow x_{i+1 (\mathrm{mod}\ 5)}$ $(i = 1, \cdots, 5)$ and of a tree: $x_j \hookrightarrow x_{j+1, j+3}$ $(j = 1, 2)$, where the estimated slope values are color-coded. Results of a statistical analysis of the accuracy and reliability of the determined causal interactions are presented in SI Section III. Time series of length 5000 are used in all these simulations. The embedding parameters are $\tau_s = 1$ and $d_s = 3$ with $s = x_1, \cdots, x_5$.

show the results from ecological networks of five mutually interacting species on a ring and on a tree structure, respectively, where the color-coded slope values reflect accurately the interaction patterns in both cases.

The second example is the coupled Lorenz system: $\dot{x}_i = \sigma_i(y_i - x_i) + \mu_{ij} x_j$, $\dot{y}_i = x_i(\rho_i - z_i) - y_i$, $\dot{z}_i = x_i y_i - \beta_i z_i$ with $i, j = 1, 2$ and $i \neq j$. We use time series $\{y_{1,t}, y_{2,t}\}_{t=n\omega}$ for detecting different configurations of causation (see Section III of SI). Figure 4 presents the overall result, where the color-coded estimated values of the slope from the continuity scaling are shown for different combinations of the sampling rate $1/\omega$ and coupling strength. Even with relatively low sampling rate, our continuity scaling framework can successfully detect and quantify the strength of causation. Note that the accuracy does not vary monotonously with the sampling rate, indicating the potential of our framework to ascertain and quantify causation even with rare data. Moreover, the proposed index can accurately reflect the true causal strength (denoting by the coupling parameter), which is also evidenced by numerical tests in Sections III and IV of SI. Robustness tests against different noise perturbations are provided in Section III of SI demonstrating the practical usefulness of our framework. Additionally, analogous to the first example, we present in SI several examples on causation detection in the coupled Lorenz system with nonlinear couplings, and the Rössler-Lorenz system, etc., which further demonstrates the generic efficacy of our framework.

In addition, we present study on several real-world dataset, which brings new insights to the evolutionary mechanism of underlying systems. We study gene expression data from DREAM4 in silico Network Challenge [47, 48], whose intrinsic gene regulatory networks (GRNs) are known for verification (Figure 5(a) and Figure S17 of SI). Applying

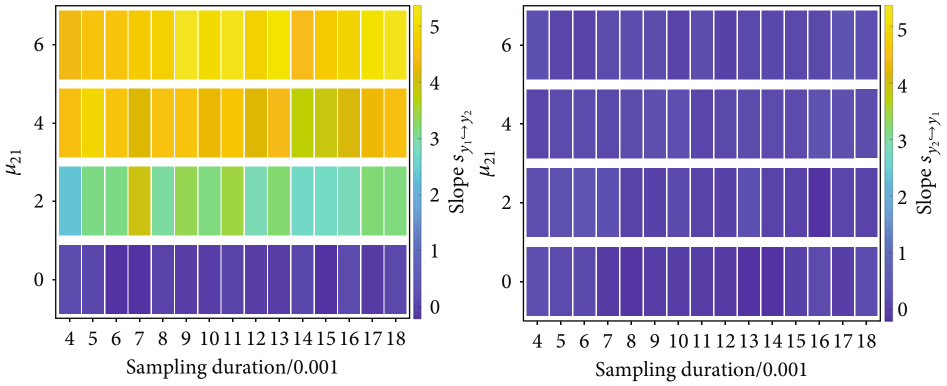

(a)

(b)

Figure 4: Detecting causation in the unidirectionally coupled Lorenz system. The results are for different values of μ_{21} ($\mu_{12}=0$) and sampling rate $1/\omega$. (a, b) Color-coded values of the slopes $s_{y_1\hookrightarrow y_2}$ and $s_{y_2\hookrightarrow y_1}$, respectively. The integration time step is 10^{-3} and the embedding parameters are $d_s=7$, $\tau_s\approx 0.05$ with $\omega|\tau_s$ ($s=y_1$ or y_2). See Section III and Table S9 of SI for all the other parameters including the time series lengths used in the simulations.

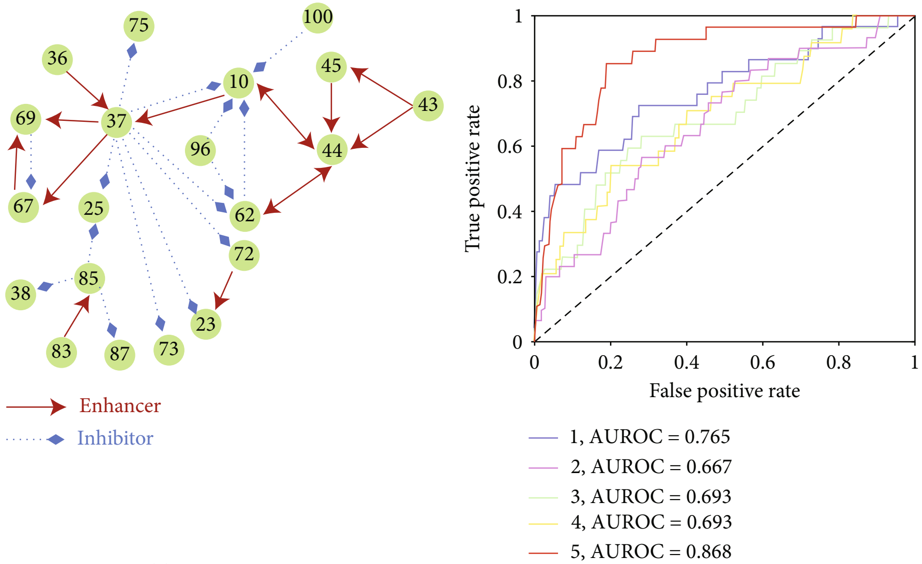

(a)

(b)

Figure 5: Detecting causal interactions in five GRNs. (a) One representative GRN containing 20 randomly selected genes. Other four structures can be found in Figure S17 of SI. (b) The ROC curves as well as their AUROC values demonstrate the efficacy of our framework.

our framework to these data, we ascertain the causations between each pair of genes by using the continuity scaling framework. The corresponding ROC curves for five different networks as well as their AUROC values are shown in Figure 5(b), which indicates a high detection accuracy in dealing with real-world data.

We then test the causal relationship in a marine ecosystem consisting of Pacific sardine landings, northern anchovy landings and sea surface temperature (SST). We reveal new findings to support the competing relationship hypothesis stated in [49] which cannot be detected by CCM [25]. As pointed out in Figure 6, while common influence from SST to both species is verified with both methods, our continuity scaling additionally illuminates notable influence from anchovy to sardine with its reverse direction being less significant. While competing relationship plays an important role in ecosystems, continuity scaling can reveal more essential interaction mechanism. See Section III.E of SI for more details.

Moreover, we study the transmission mechanism of the recent COVID-19 pandemic. Particularly, we analyze the daily new cases of COVID-19 of representative countries for two stages: day 1 (January 22 nd 2020) to day 100 (April 30 th 2020) and day 101 (May 1 st 2020) to day 391 (February 15 th 2021). Our continuity scaling is pairwisely applied to reconstruct the transmission causal network. As shown in Figure 7, China shows a significant effect on a few countries at the first stage and this effect disappears at the second stage. However, other countries show a different situation with China, whose external effect lasts as shown in Section III.E and Figure S18 of SI. Our results accord with that China holds stringent epidemic control strategies with

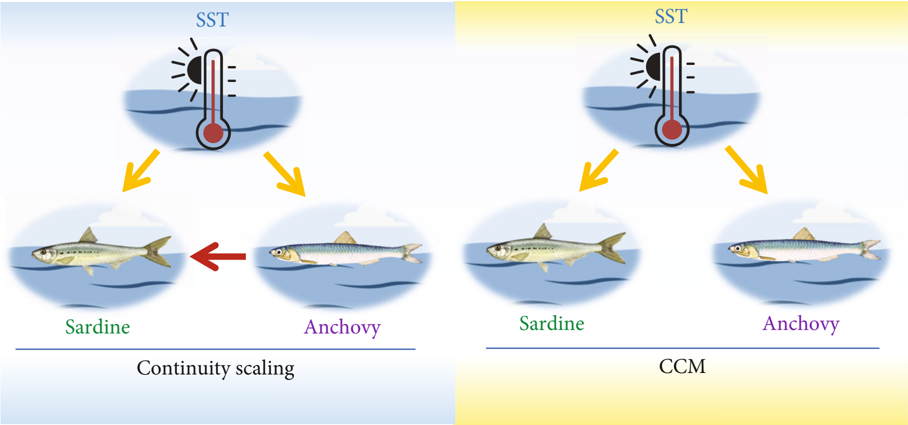

Figure 6: The comparison of causal network structure detected by continuity scaling and CCM among sea surface temperature, sardine, and anchovy.

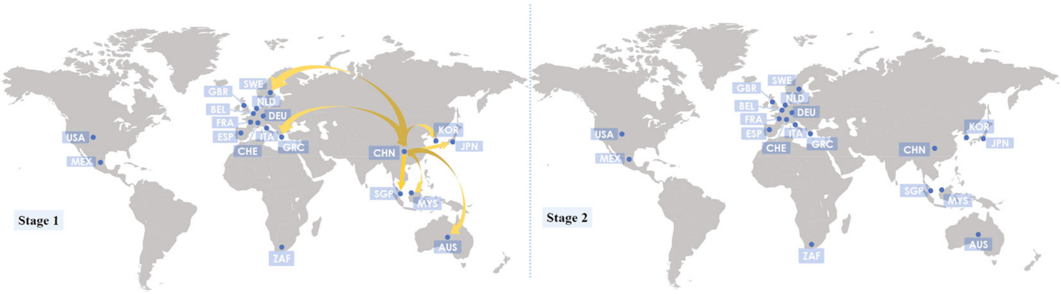

Figure 7: The causal effect from China to other countries of the COVID-19 pandemic detected by continuity scaling between stages 1 and 2. Here, stage 1 is from January 22nd 2020 to April 30th 2020, and stage 2 is from May 1st 2020 to February 15th 2021. For those detected causal links between all countries, refer to Section III.E and Figure S18 of SI. These maps are for illustration only.

sporadic domestic infections, as evidenced by official daily briefings, demonstrating the potential of continuity scaling in detecting causal networks for ongoing complex systems. Additionally, We emphasize that day 100 is a suitable critical day to distinguish the early severe stage and the late well-under-control stage of the pandemic (see Figure S18(a) of SI), while slight change of the critical day will not nullify our result. As shown in Figure S18(b) of SI, when the critical day varies from day 94 to day 106, no significant change (less than 5%) of the detected causal links occurs at both stages, and the number of countries under influence of China at Stage 2 remains zero. See more details in Section III.E of SI.

Additional real world examples including air pollutants and hospital admission record from Hong Kong are also shown in Section III of SI.

4. Discussion

To summarize, we have developed a novel framework for data-based detection and quantification of causation in complex dynamical systems. On the basis of the widely used cross-map-based techniques, our framework enjoys a rigorous foundation, focusing on the continuity scaling law of the concerned system directly instead of only investigating the continuity of its cross-map. Therefore, our framework is consistent with the standard interpretation of causality, and works even in the typical cases where several existing typical methods do not perform that well or even they fail (see the comparison results in Section IV of SI). In addition, the mathematical reasoning leading to the core of our framework, the continuity scaling, helps resolve the long-standing issue associated with techniques directly using cross-map that information about the resulting variables is required to project the dynamical behavior of the causal variables, whereas several works in the literature [50], which directly studied the continuity or the smoothness of the cross-map, likely yielded confused detected results on causal directions.

Computational complexity. The computational complexity of the algorithm is $O(T^2 N_\varepsilon)$, which is relatively smaller than the CCM method, whose computational complexity is $O(T^2 \log T)$.

Limitations and future works. Nevertheless, there are still some spaces for improving the presently proposed framework. First, currently, only bivariate detection algorithm is designed, so generalization to multivariate network inference requires further considerations, as analogous to those works presented in Refs. [51–53]. Second, the causal time delay has not been taken into account in the current framework, so it also could be further investigated, similar to the work reported in Ref. [33]. Also, more advanced algorithms, such as the one developed in Ref. [54], could be integrated into this framework for detecting those temporal causal structures. Definitely, we will settle these questions in our future work.

Detecting causality in complex dynamical systems has broad applications not only in science and engineering, but also in many aspects of the modern society, demanding accurate, efficient, and rigorously justified and hence trustworthy methodologies. Our present work provides a vehicle along this feat and indeed resolves the puzzles arising in the use of those influential methods.

5. Methods

Continuity scaling framework: a detailed description of algorithms. Let $\{u_t\}_{t=1,2,\cdots,T}$ and $\{v_t\}_{t=1,2,\cdots,T}$ be two experimentally measured time series of internal variables $\{(\mathrm{x}_t, \mathrm{y}_t)\}_{t\in\mathbb{N}}$. Typically, if the dynamical variables $\{(\mathrm{x}_t, \mathrm{y}_t)\}_{t\in\mathbb{N}}$ are accessible, $\{(u_t, v_t)\}$ reduce to one-dimensional coordinate of the internal system. The key computational steps of our continuity scaling framework are described, as follows.

We reconstruct the phase space using the classical method of delay coordinate embedding [37] with the optimal embedding dimension d_z and time lag τ_z determined by the methods in Refs. [55, 56] (i.e., the false nearest neighbors and the delayed mutual information, respectively):

$$\mathscr{L}_z \triangleq \left\{\mathbf{z}(t) = \left(z_t, z_{t+\tau_z}, \cdots, z_{t+(d_z-1)\tau_z}\right) | t = 1, \cdots, T_0\right\}, \quad (6)$$

where $z = u, v$, $T_0 = \min\{T - (d_z - 1)\tau_z | z = u, v\}$, and Euclidean distance is used for both $\mathscr{L}_{u,v}$.

We present the steps for causation detection using the case of $\mathbf{v}\hookrightarrow\mathbf{u}$ as an example.

We calculate the respective diameters for $\mathscr{L}_{u,v}$ as

$$D_z \triangleq \max\left\{\mathrm{dist}_{\mathscr{L}_z}(\mathbf{z}(t), \mathbf{z}(\tau)) | 1 \le t, \tau \le T_0\right\}, \quad (7)$$

where $z = u, v$, and $\mathbf{z} = \mathbf{u}, \mathbf{v}$. We set up a group of numbers, $\{\varepsilon_{\mathbf{u},j}\}_{j=1,\cdots,N_\varepsilon}$, as $\varepsilon_{\mathbf{u},1} = e \cdot D_u$, $\varepsilon_{\mathbf{u},N_\varepsilon} = D_u$, with the other elements satisfying

$$\frac{\ln \varepsilon_{\mathbf{u},j} - \ln \varepsilon_{\mathbf{u},1}}{j-1} = \frac{\ln \varepsilon_{\mathbf{u},N_\varepsilon} - \ln \varepsilon_{\mathbf{u},1}}{N_\varepsilon - 1}, \quad (8)$$

for $j = 2, \cdots, N_\varepsilon - 1$. Then, in light of (2) with (3), we have

$$\delta^t_{\mathbf{v}}(\varepsilon_{\mathbf{u}}) = \#\left[I^t_{\mathbf{u}}(\varepsilon_{\mathbf{u}})\right]^{-1} \sum_{\tau\in I^t_{\mathbf{u}}(\varepsilon_{\mathbf{u}})} \mathrm{dist}_{\mathscr{L}_v}(\mathbf{v}(t), \mathbf{v}(\tau-1)), \quad (9)$$

with

$$I^t_{\mathbf{u}}(\varepsilon_{\mathbf{u}}) = \left\{\tau \in \mathbb{N} \middle| \mathrm{dist}_{\mathscr{L}_u}(\mathbf{u}(t+1), \mathbf{u}(\tau)) < \varepsilon_{\mathbf{u}}, |t+1-\tau| > E\right\} \quad (10)$$

where numerically, $\varepsilon_{\mathbf{u}}$ alters its value successively from the set $\{\varepsilon_{\mathbf{u},j}\}_{j=1,\cdots,N_\varepsilon}$, and the threshold E is a positive number chosen to avoid the situation where the nearest neighboring points are induced by the consecutive time order only.

As defined, $\langle\delta^t_{\mathbf{v}}(\varepsilon_{\mathbf{u}})\rangle_{t\in\mathbb{N}}$ is the average of $\delta^t_{\mathbf{v}}(\varepsilon_{\mathbf{u}})$ over all possible time t. We use a finite number of pairs $\{(\langle\delta^t_{\mathbf{v}}(\varepsilon_{\mathbf{u},j})\rangle_{t\in\mathbb{N}_{T_0}}, \ln \varepsilon_{\mathbf{u},j})\}_{j=1,\cdots,N_\varepsilon}$ to approximate the scaling relation between $\langle\delta^t_{\mathbf{v}}(\varepsilon_{\mathbf{u}})\rangle_{t\in\mathbb{N}}$ and $\ln \varepsilon_{\mathbf{u}}$, where $\mathbb{N}_{T_0} = \{1, 2, \cdots, T_0\}$. Theoretically, a larger value of N_ε and a smaller value of e will result in a more accurate approximation of the scaling relation. In practice, the accuracy is determined by the length of the observational time series, the sampling duration, and different types of noise perturbations. In numerical simulations, we set $e = 0.001$ and $N_\varepsilon = 33$. In addition, a too large or a too small value of $\varepsilon_{\mathbf{u}}$ can induce insufficient data to restore the neighborhood and/or the entire manifold. We thus set $\delta^t_{\mathbf{v}}(\varepsilon_{\mathbf{u},j}) = \delta^t_{\mathbf{v}}(\varepsilon_{\mathbf{u},j+1})$ as a practical technique as the number of points is limited practically in a small neighborhood. As a result, near zero slope values would appear on both sides of the scaling curve $\langle\delta^t_{\mathbf{v}}(\varepsilon_{\mathbf{u}})\rangle_{t\in\mathbb{N}}$-$\ln \varepsilon_{\mathbf{u}}$, as demonstrated in Figure 3 and in SI. In such a case, to estimate the slope of the scaling relation, we take the following approach.

Define a group of numbers by

$$S_j \triangleq \frac{\left\langle\delta^t_{\mathbf{v}}\left(\varepsilon_{\mathbf{u},j+1}\right)\right\rangle_{t\in\mathbb{N}_{T_0}} - \left\langle\delta^t_{\mathbf{v}}\left(\varepsilon_{\mathbf{u},j}\right)\right\rangle_{t\in\mathbb{N}_{T_0}}}{\ln \varepsilon_{\mathbf{u},j+1} - \ln \varepsilon_{\mathbf{u},j}}, \quad (11)$$

where $j = 1, \cdots, N_\varepsilon - 1$, sort them in a descending order, from which we determine the $[N_\varepsilon + 1/2]$ largest numbers, collect their subscripts - j's together as an index set $\widehat{J}$, and set $H \triangleq \{j, j+1 | j \in \widehat{J}\}$. Applying the least squares method to the linear regression model:

$$\left\langle\delta^t_{\mathbf{v}}(\varepsilon_{\mathbf{u}})\right\rangle_{t\in\mathbb{N}} = S \cdot \ln \varepsilon_{\mathbf{u}} + b \quad (12)$$

with the dataset $\{(\langle\delta^t_{\mathbf{v}}(\varepsilon_{\mathbf{u},j})\rangle_{t\in\mathbb{N}_{T_0}}, \ln \varepsilon_{\mathbf{u},j})\}_{j\in H}$, we get the optimal values $(\widehat{S}, \widehat{b})$ for the parameters (S, b) in (12) and finally obtain the slope of the scaling relation as $s_{\mathbf{v}\hookrightarrow\mathbf{u}} \triangleq \widehat{S}$.

For the other causal direction from $\mathbf{u}$ to $\mathbf{v}$, these steps are equally applicable to estimating the slope $s_{\mathbf{u}\hookrightarrow\mathbf{v}}$.

To assess the statistical significance of the numerically determined causation, we devise the following surrogate test using the case of $\mathbf{v}$ causing $\mathbf{u}$ as an illustrative example.

Divide the time series $\{\mathbf{u}(t)\}_{t\in\mathbb{N}_{T_0}}$ into N_G consecutive segments of equal length (except for the last segment - the shortest segment). Randomly shuffle these segments and then regroup them into a surrogate sequence $\{\widehat{\mathbf{u}}(t)\}_{t\in\mathbb{N}_{T_0}}$. Applying such a random permutation method to $\{\mathbf{v}(t)\}_{t\in\mathbb{N}_{T_0}}$ generates another surrogate sequence $\{\widehat{\mathbf{v}}(t)\}_{t\in\mathbb{N}_{T_0}}$. Carrying out the slope computation yields $s_{\widehat{\mathbf{v}}\hookrightarrow\widehat{\mathbf{u}}}$. The procedure can be repeated for a sufficient number of times, say Q, which consequently yields a group of estimated slopes, denoted as $\{s^q_{\widehat{\mathbf{v}}\hookrightarrow\widehat{\mathbf{u}}}\}_{q=0,1\cdots,Q}$, where $s^0_{\widehat{\mathbf{v}}\hookrightarrow\widehat{\mathbf{u}}}$ is set as $s_{\mathbf{v}\hookrightarrow\mathbf{u}}$ obtained from the original time series. For all the estimated slopes, we calculate their mean $\widehat{\mu}_{\mathbf{v}\hookrightarrow\mathbf{u}}$ and the standard deviation $\widehat{\sigma}_{\mathbf{v}\hookrightarrow\mathbf{u}}$. The p-value for $s_{\mathbf{v}\hookrightarrow\mathbf{u}}$ is calculated as

$$p_{s_{\mathbf{v}\hookrightarrow\mathbf{u}}} \triangleq 1 - \operatorname{normcdf}\left[\frac{s_{\mathbf{v}\hookrightarrow\mathbf{u}} - \widehat{\mu}_{\mathbf{v}\hookrightarrow\mathbf{u}}}{\widehat{\sigma}_{\mathbf{v}\hookrightarrow\mathbf{u}}}\right], \tag{13}$$

where $\operatorname{normcdf}[\cdot]$ is the cumulative Gaussian distribution function. The principle of statistical hypothesis testing guarantees the existence of causation from $\mathbf{v}$ to $\mathbf{u}$ if $p_{s_{\mathbf{v}\hookrightarrow\mathbf{u}}} < 0.05$.

In simulations, we set the number of segments to be $N_G = 25$ and the number of times for random permutations to be $Q \geq 20$.

Additional Points

Code Availability. The source codes for our CS framework are available at https://github.com/bianzhiyu/ContinuityScaling.

Conflicts of Interest

The authors declare no competing interests.

Authors' Contributions

W.L. conceived idea. X.Y., S.-Y.L., and W.L. designed and performed the research. X.Y., S.-Y.L., H.-F.M., and W.L. analyzed the data. H.-F.M., Y.-C.L., and Q.N. contributed data and analysis tools, and all the authors wrote the paper. X.Y. and S.-Y.L. equally contributed to this work.

Acknowledgments

W.L. is supported by the National Key R&D Program of China (Grant No. 2018YFC0116600), by the National Natural Science Foundation of China (Grant Nos. 11925103 and 61773125), by the STCSM (Grant No. 18DZ1201000), and by the Shanghai Municipal Science and Technology Major Project (No. 2021SHZDZX0103). Y.-C.L. is supported by AFOSR (Grant No. FA9550-21-1-0438). S.-Y.L. is supported by the National Natural Science Foundation of China (No. 12101133) and "Chenguang Program" supported by Shanghai Education Development Foundation and Shanghai Municipal Education Commission (No. 20CG01). Q.N. is partially supported by NSF (Grant No. DMS1763272) and the Simons Foundation (Grant No. 594598). H.-F.M. is supported by the National Natural Science Foundation of China (Grant No. 12171350) and by the National Key R&D Program of China (Grant No. 2018YFA0801100).

Supplementary Materials

Supplementary materials: SI.pdf (where we include analytic and computational details of the results in the main text. This SI is helpful but not essential for understanding the main results of the paper.) *(Supplementary Materials)*

References

[1] M. Bunge, *Causality and Modern Science*, Routledge, 2017.

[2] J. Pearl, *Causality*, Cambridge university press, 2013.

[3] J. Runge, S. Bathiany, E. Bollt et al., "Inferring causation from time series in earth system sciences," *Nature Communications*, vol. 10, no. 1, p. 2553, 2019.

[4] F. S. Collins and H. Varmus, "A new initiative on precision medicine," *New England Journal of Medicine*, vol. 372, no. 9, pp. 793–795, 2015.

[5] G. N. Saxe, A. Statnikov, D. Fenyo et al., "A complex systems approach to causal discovery in psychiatry," *PloS One*, vol. 11, no. 3, article e0151174, 2016.

[6] D. R. Cox and D. V. Hinkley, *Theoretical Statistics*, CRC Press, 1979.

[7] T. M. Cover, *Elements of Information Theory*, John Wiley & Sons, 1999.

[8] J. Pearl, "Causal inference in statistics: an overview," *Statistics Surveys*, vol. 3, pp. 96–146, 2009.

[9] N. Wiener, *The Theory of Prediction*, Modern mathematics for engineers, 1956.

[10] C. W. Granger, "Investigating causal relations by econometric models and cross-spectral methods," *Econometrica: Journal of the Econometric Society*, vol. 37, no. 3, pp. 424–438, 1969.

[11] S. Haufe, V. V. Nikulin, K. R. Müller, and G. Nolte, "A critical assessment of connectivity measures for EEG data: a simulation study," *NeuroImage*, vol. 64, pp. 120–133, 2013.

[12] M. Ding, Y. Chen, and S. L. Bressler, "Granger causality: basic theory and application to neuroscience," *Handbook of Time Series Analysis: recent theoretical developments and applications*, vol. 437, 2006.

[13] T. Schreiber, "Measuring information transfer," *Physical Review Letters*, vol. 85, no. 2, pp. 461–464, 2000.

[14] S. Frenzel and B. Pompe, "Partial mutual information for coupling analysis of multivariate time series," *Physical Review Letters*, vol. 99, no. 20, article 204101, 2007.

[15] R. Vicente, M. Wibral, M. Lindner, and G. Pipa, "Transfer entropy–a model-free measure of effective connectivity for the neurosciences," *Journal of Computational Neuroscience*, vol. 30, no. 1, pp. 45–67, 2011.

[16] J. Runge, J. Heitzig, V. Petoukhov, and J. Kurths, "Escaping the curse of dimensionality in estimating multivariate transfer entropy," *Physical Review Letters*, vol. 108, no. 25, article 258701, 2012.

[17] J. Sun, C. Cafaro, and E. M. Bollt, "Identifying the coupling structure in complex systems through the optimal causation entropy principle," *Entropy*, vol. 16, no. 6, pp. 3416–3433, 2014.

[18] C. Cafaro, W. M. Lord, J. Sun, and E. M. Bollt, "Causation entropy from symbolic representations of dynamical systems," *Chaos: An Interdisciplinary Journal of Nonlinear Science*, vol. 25, article 043106, 2015.

[19] J. Sun, D. Taylor, and E. M. Bollt, "Causal network inference by optimal causation entropy," *SIAM Journal on Applied Dynamical Systems*, vol. 14, no. 1, pp. 73–106, 2015.

[20] M. Solyanik-Gorgone, J. Ye, M. Miscuglio, A. Afanasev, A. E. Willner, and V. J. Sorger, "Quantifying information via Shannon entropy in spatially structured optical beams," *Research*, vol. 2021, article 9780760, 2021.

[21] Y. Hirata and K. Aihara, "Identifying hidden common causes from bivariate time series: a method using recurrence plots," *Physical Review E*, vol. 81, no. 1, article 016203, 2010.

[22] R. Q. Quiroga, J. Arnhold, and P. Grassberger, “Learning driver-response relationships from synchronization patterns,” *Physical Review E*, vol. 61, no. 5, pp. 5142–5148, 2000.

[23] J. Arnhold, P. Grassberger, K. Lehnertz, and C. E. Elger, “A robust method for detecting interdependences: application to intracranially recorded eeg,” *Physica D: Nonlinear Phenomena*, vol. 134, no. 4, pp. 419–430, 1999.

[24] D. Harnack, E. Laminski, M. Schünemann, and K. R. Pawelzik, “Topological causality in dynamical systems,” *Physical Review Letters*, vol. 119, no. 9, article 098301, 2017.

[25] G. Sugihara, R. May, H. Ye et al., “Detecting causality in complex ecosystems,” *Science*, vol. 338, no. 6106, pp. 496–500, 2012.

[26] E. R. Deyle, M. Fogarty, C. H. Hsieh et al., “Predicting climate effects on pacific sardine,” *Proceedings of the National Academy of Sciences*, vol. 110, no. 16, pp. 6430–6435, 2013.

[27] X. Wang, S. Piao, P. Ciais et al., “A two-fold increase of carbon cycle sensitivity to tropical temperature variations,” *Nature*, vol. 506, no. 7487, pp. 212–215, 2014.

[28] H. Ma, K. Aihara, and L. Chen, “Detecting causality from nonlinear dynamics with short-term time series,” *Scientific Reports*, vol. 4, pp. 1–10, 2014.

[29] J. M. McCracken and R. S. Weigel, “Convergent cross-mapping and pairwise asymmetric inference,” *Physical Review E*, vol. 90, no. 6, article 062903, 2014.

[30] H. Ye, E. R. Deyle, L. J. Gilarranz, and G. Sugihara, “Distinguishing time-delayed causal interactions using convergent cross mapping,” *Scientific Reports*, vol. 5, no. 1, article 14750, 2015.

[31] A. T. Clark, H. Ye, F. Isbell et al., “Spatial convergent cross mapping to detect causal relationships from short time series,” *Ecology*, vol. 96, no. 5, pp. 1174–1181, 2015.

[32] J.-J. Jiang, Z.-G. Huang, L. Huang, H. Liu, and Y.-C. Lai, “Directed dynamical influence is more detectable with noise,” *Scientific Reports*, vol. 6, no. 1, article 24088, 2016.

[33] H. Ma, S. Leng, C. Tao et al., “Detection of time delays and directional interactions based on time series from complex dynamical systems,” *Physical Review E*, vol. 96, no. 1, article 012221, 2017.

[34] J. M. Amigó and Y. Hirata, “Detecting directional couplings from multivariate flows by the joint distance distribution,” *Chaos: An Interdisciplinary Journal of Nonlinear Science*, vol. 28, article 075302, 2018.

[35] Y. Wang, J. Yang, Y. Chen, P. De Maeyer, Z. Li, and W. Duan, “Detecting the causal effect of soil moisture on precipitation using convergent cross mapping,” *Scientific Reports*, vol. 8, no. 1, pp. 1–8, 2018.

[36] S. Leng, H. Ma, J. Kurths et al., “Partial cross mapping eliminates indirect causal influences,” *Nature Communications*, vol. 11, no. 1, pp. 1–9, 2020.

[37] F. Takens, “Detecting strange attractors in turbulence,” in *Dynamical Systems and Turbulence, Warwick 1980*, Springer, 1981.

[38] N. H. Packard, J. P. Crutchfield, J. D. Farmer, and R. S. Shaw, “Geometry from a time series,” *Physical Review Letters*, vol. 45, no. 9, pp. 712–716, 1980.

[39] T. Sauer, J. A. Yorke, and M. Casdagli, “Embedology,” *Journal of Statistical Physics*, vol. 65, no. 3-4, pp. 579–616, 1991.

[40] J. Stark, “Delay embeddings for forced systems. I. Deterministic forcing,” *Journal of Nonlinear Science*, vol. 9, no. 3, pp. 255–332, 1999.

[41] J. Stark, D. S. Broomhead, M. E. Davies, and J. Huke, “Delay embeddings for forced systems. II. Stochastic forcing,” *Journal of Nonlinear Science*, vol. 13, no. 6, pp. 519–577, 2003.

[42] M. R. Muldoon, D. S. Broomhead, J. P. Huke, and R. Hegger, “Delay embedding in the presence of dynamical noise,” *Dynamics and Stability of Systems*, vol. 13, no. 2, pp. 175–186, 1998.

[43] P. Spirtes, C. N. Glymour, R. Scheines, and D. Heckerman, *Causation, Prediction, and Search*, MIT press, 2001.

[44] B. Cummins, T. Gedeon, and K. Spendlove, “On the efficacy of state space reconstruction methods in determining causality,” *SIAM Journal on Applied Dynamical Systems*, vol. 14, no. 1, pp. 335–381, 2015.

[45] H. Kantz and T. Schreiber, *Nonlinear Time Series Analysis*, vol. 7, Cambridge university press, 2004.

[46] G. Lancaster, D. Iatsenko, A. Pidde, V. Ticcinelli, and A. Stefanovska, “Surrogate data for hypothesis testing of physical systems,” *Physics Reports*, vol. 748, pp. 1–60, 2018.

[47] D. Marbach, T. Schaffter, C. Mattiussi, and D. Floreano, “Generating realistic in silico gene networks for performance assessment of reverse engineering methods,” *Journal of Computational Biology*, vol. 16, no. 2, pp. 229–239, 2009.

[48] D. Marbach, R. J. Prill, T. Schaffter, C. Mattiussi, D. Floreano, and G. Stolovitzky, “Revealing strengths and weaknesses of methods for gene network inference,” *Proceedings of the National Academy of Sciences*, vol. 107, no. 14, pp. 6286–6291, 2010.

[49] R. Lasker and A. Mac Call, “New ideas on the fluctuations of the clupeoid stocks off California,” *Proceedings of the Joint Oceanographic Assembly, Halifax, August 1982: General Symposia*, Department of Fisheries and Oceans, Ontario, 1983.

[50] M. L. V. Quyen, J. Martinerie, C. Adam, and F. J. Varela, “Nonlinear analyses of interictal EEG map the brain interdependences in human focal epilepsy,” *Physica D: Nonlinear Phenomena*, vol. 127, no. 3-4, pp. 250–266, 1999.

[51] J. Peters, D. Janzing, and B. Schölkopf, *Elements of Causal Inference: Foundations and Learning Algorithms*, MIT Press, 2017.

[52] J. Runge, “Causal network reconstruction from time series: from theoretical assumptions to practical estimation,” *Chaos: An Interdisciplinary Journal of Nonlinear Science*, vol. 28, article 075310, 2018.

[53] Y. Lou, L. Wang, and G. Chen, “Enhancing controllability robustness of q-snapback networks through redirecting edges,” *Research*, vol. 2019, article 7857534, 23 pages, 2019.

[54] J.-W. Hou, H.-F. Ma, D. He, J. Sun, Q. Nie, and W. Lin, “Harvesting random embedding for high-frequency change-point detection in temporal complex,” *National Science Review*, vol. 9, article nwab228, 2022.

[55] A. M. Fraser and H. L. Swinney, “Independent coordinates for strange attractors from mutual information,” *Physical Review A*, vol. 33, no. 2, pp. 1134–1140, 1986.

[56] M. B. Kennel, R. Brown, and H. D. Abarbanel, “Determining embedding dimension for phase-space reconstruction using a geometrical construction,” *Physical Review A*, vol. 45, no. 6, pp. 3403–3411, 1992.

Supplementary Information for "Continuity scaling: A rigorous framework for detecting and quantifying causality accurately"

Xiong Ying,[1,2,3] Si-Yang Leng,[2,4] Huan-Fei Ma,[5]
Qing Nie,[6] Ying-Cheng Lai,[7] and Wei Lin[1,2,3,8,*]

[1]*School of Mathematical Sciences, SCMS, and SCAM,*
Fudan University, Shanghai 200433, China
[2]*Research Institute for Intelligent Complex Systems, CCSB,*
and LCNBI, Fudan University, Shanghai 200433, China
[3]*State Key Laboratory of Medical Neurobiology,*
and MOE Frontiers Center for Brain Science,
Institutes of Brain Science, Fudan University, Shanghai 200032, China
[4]*Institute of AI and Robotics, Academy for Engineering and Technology,*
Fudan University, Shanghai 200433, China
[5]*School of Mathematical Sciences, Soochow University, Suzhou 215006, China*
[6]*Department of Mathematics, Department of Developmental and Cell Biology,*
and NSF-Simons Center for Multiscale Cell Fate Research,
University of California, Irvine, CA 92697-3875, USA
[7]*School of Electrical, Computer, and Energy Engineering,*
Arizona State University, Tempe, Arizona 85287-5706, USA
[8]*Shanghai Artificial Intelligence Laboratory, Shanghai 200232, China*

(Dated: March 23, 2022)

Abstract

The Supplementary Information provides analytic and computational details of the results in the main text. It is helpful but not essential for understanding the main results of the paper. The materials are organized as

CONTENTS

---

* wlin@fudan.edu.cn

I. MATHEMATICAL NOTATIONS

Listed in Tab. S1 are mathematical notations used in this work.

TABLE S1. Illustrations on notations.

Notations	Illustrations
$\boldsymbol{x}_t,\ \boldsymbol{y}_t$	Internal states of the original dynamical system at time t evolving on some compact manifold.
$u(\cdot),\ v(\cdot)$	Observational functions, either depending on only partial Cartesian coordinates of the state variables $\boldsymbol{x}$ and $\boldsymbol{y}$, respectively, or containing mixed information from the state variables.
$u_t,\ v_t$	Values of the observational functions from the internal states of the original dynamical system at time t.
$\boldsymbol{u}_t,\ \boldsymbol{v}_t$	Reconstructed state vectors at time t consisting of the delayed coordinates based on the observational time series $\{u_t\}_{t\in\mathbb{N}}$ and $\{v_t\}_{t\in\mathbb{N}}$, respectively.
$\varepsilon_{\boldsymbol{u}}$	Radius of the neighborhood on the manifold where the variable $\boldsymbol{u}$ is assumed to represent an effect.
$\delta^t_{\boldsymbol{v}}(\varepsilon_{\boldsymbol{u}})$	Radius of the pull-back neighborhood on the manifold where $\boldsymbol{v}$ is supposed to be a causal variable, which corresponds to the neighborhood of radius $\varepsilon_{\boldsymbol{u}}$. Here, time t indicates the point at which the estimation of the radius is applicable.
$\langle\delta^t_{\boldsymbol{v}}(\varepsilon_{\boldsymbol{u}})\rangle_{t\in\mathbb{N}}$	The average of $\delta^t_{\boldsymbol{v}}(\varepsilon_{\boldsymbol{u}})$ over all possible time t for a given number $\varepsilon_{\boldsymbol{u}}$.
$s_{\boldsymbol{v}\hookrightarrow\boldsymbol{u}}$	Estimated slope of the regression line obtained from the scaling relation between $\langle\delta^t_{\boldsymbol{v}}(\varepsilon_{\boldsymbol{u}})\rangle_t$ and $\ln\varepsilon_{\boldsymbol{u}}$.

II. ESTIMATING RADIUS OF NEIGHBORHOOD AND SCALING LAW

We rewrite the considered original dynamical system here as

$$\boldsymbol{x}_{t+1}=\boldsymbol{f}(\boldsymbol{x}_t,\boldsymbol{y}_t),\quad \boldsymbol{y}_{t+1}=\boldsymbol{g}(\boldsymbol{x}_t,\boldsymbol{y}_t),\quad t\in\mathbb{N},\tag{S2.1}$$

where $\{\boldsymbol{x}_t\}_{t\in\mathbb{N}}$ and $\{\boldsymbol{y}_t\}_{t\in\mathbb{N}}$ evolve on compact manifolds $\mathcal{M}$, $\mathcal{N}$ of dimension $D_{\mathcal{M}}$, $D_{\mathcal{N}}$ respectively and $[\boldsymbol{f},\boldsymbol{g}]$ are sufficiently smooth map functions. The internal states $\{\boldsymbol{x}_t,\boldsymbol{y}_t\}_{t\in\mathbb{N}}$ of system (S2.1) are either completely or partially accessible and $\{u_t,v_t\}_{t\in\mathbb{N}}$ are the two observational time series. Let $u_t=u(\boldsymbol{x}_t)$ and $v_t=v(\boldsymbol{y}_t)$. With the embedding dimensions $d_{u,v}$ and delay time $\tau_{u,v}$ properly chosen according to some empirical criteria (See Methods in the main text), we reconstruct the state vectors as $\boldsymbol{z}_t=(z_t,z_{t+\tau_z},\ldots,z_{t+(d_z-1)\tau_z})$, where $\boldsymbol{z}=\boldsymbol{u},\boldsymbol{v}$ and $z=u,v$. The dynamical evolution of the reconstructed state vectors is governed by

$$\boldsymbol{u}_{t+1}=\tilde{\boldsymbol{f}}(\boldsymbol{u}_t,\boldsymbol{v}_t),\quad \boldsymbol{v}_{t+1}=\tilde{\boldsymbol{g}}(\boldsymbol{u}_t,\boldsymbol{v}_t),\quad t\in\mathbb{N},\tag{S2.2}$$

where $\boldsymbol{u}_t\in\mathcal{L}_u$ and $\boldsymbol{v}_t\in\mathcal{L}_v$. When the observational functions so defined are identity functions, the explicit intrinsic states of the original system are recovered: $\boldsymbol{u}=\boldsymbol{x}$ and

$\boldsymbol{v} = \boldsymbol{y}$. The mathematical reasoning below is thus not only suitable for the more general Case II defined in the main text, but also for Case I through a direct substitution of $\boldsymbol{u}$ and $\boldsymbol{v}$ by $\boldsymbol{x}$ and $\boldsymbol{y}$, respectively.

For a given $\boldsymbol{u}_g \in \mathcal{L}_u$, we set $\tilde{\boldsymbol{f}}_{\boldsymbol{u}_g}(\cdot) \triangleq \tilde{\boldsymbol{f}}(\boldsymbol{u}_g, \cdot)$. For any given $\varepsilon_{\boldsymbol{u}} > 0$, we examine the preimage of the neighborhood $\mathcal{O}(\boldsymbol{u}_{t+1}, \varepsilon_{\boldsymbol{u}})$. Denoting this pull-back neighborhood as $\tilde{\boldsymbol{f}}^{-1}_{\boldsymbol{u}_t}(\mathcal{O}(\boldsymbol{u}_{t+1}, \varepsilon_{\boldsymbol{u}}))$, we have that $\tilde{\boldsymbol{f}}^{-1}_{\boldsymbol{u}_t}(\mathcal{O}(\boldsymbol{u}_{t+1}, \varepsilon_{\boldsymbol{u}}))$ is a neighborhood of $\boldsymbol{v}_t$ because of the relation $\tilde{\boldsymbol{f}}_{\boldsymbol{u}_t}(\boldsymbol{v}_t) = \boldsymbol{u}_{t+1}$ from system (S2.2). Of particular interest is *whether and how* $\tilde{\boldsymbol{f}}^{-1}_{\boldsymbol{u}_t}(\mathcal{O}(\boldsymbol{u}_{t+1}, \varepsilon_{\boldsymbol{u}}))$ contracts to the point $\boldsymbol{v}_t$ as $\varepsilon_{\boldsymbol{u}}$ tends to zero, as the existence of some scaling of this correspondent continuity is not only indicative but also a quantitative characterization of causation from $\boldsymbol{v}_t$ to $\boldsymbol{u}_t$ at time t.

To obtain the continuity scaling, for given $\varepsilon_{\boldsymbol{u}}$, we analytically define the "radius" of the neighborhood $\tilde{\boldsymbol{f}}^{-1}_{\boldsymbol{u}_t}(\mathcal{O}(\boldsymbol{u}_{t+1}, \varepsilon_{\boldsymbol{u}}))$ as

$$\delta^t_{\boldsymbol{v}}(\varepsilon_{\boldsymbol{u}}) \triangleq \left\{\mathrm{Vol}\left[\tilde{\boldsymbol{f}}^{-1}_{\boldsymbol{u}_t}(\mathcal{O}(\boldsymbol{u}_{t+1}, \varepsilon_{\boldsymbol{u}}))\right]\right\}^{-1} \int_{\tilde{\boldsymbol{f}}^{-1}_{\boldsymbol{u}_t}(\mathcal{O}(\boldsymbol{u}_{t+1}, \varepsilon_{\boldsymbol{u}}))} \mathrm{dist}_{\mathcal{L}_v}(\boldsymbol{v}, \boldsymbol{v}_t)\, \mathrm{d}\boldsymbol{v}, \tag{S2.3}$$

where $\mathrm{Vol}[\cdot]$ represents the volume of a given set. In applications, one relies on the reconstructed measured time series $\{\boldsymbol{u}_t, \boldsymbol{v}_t\}_{t\in\mathbb{N}}$ to estimate the quantity $\delta^t_{\boldsymbol{v}}(\varepsilon_{\boldsymbol{u}})$. The most accurate estimation obtained in an ideal situation is

$$\delta^t_{\boldsymbol{v}}(\varepsilon_{\boldsymbol{u}}) \triangleq \left\{\#\hat{I}(\varepsilon_{\boldsymbol{u}})\right\}^{-1} \sum_{\iota \in \hat{I}(\varepsilon_{\boldsymbol{u}})} \mathrm{dist}_{\mathcal{L}_v}(\boldsymbol{v}_t, \boldsymbol{v}_\iota), \tag{S2.4}$$

where

$$\hat{I}(\varepsilon_{\boldsymbol{u}}) \triangleq \left\{\iota \in \mathbb{N} \;\middle|\; \boldsymbol{v}_\iota \in \tilde{\boldsymbol{f}}^{-1}_{\boldsymbol{u}_t}(\mathcal{O}(\boldsymbol{u}_{t+1}, \varepsilon_{\boldsymbol{u}}))\right\} \tag{S2.5}$$

and $\#[\cdot]$ is the cardinality of a given set. However, because of lack of sufficient information about $\tilde{\boldsymbol{f}}$, in general such an estimation cannot be obtained directly. The ideal index set $\hat{I}(\varepsilon_{\boldsymbol{u}})$ defined in Eq. (S2.5) thus is usually not available.

To overcome this difficulty, we make use of the following

$$\sup_{\boldsymbol{v}\in\mathcal{L}_v} \mathrm{dist}_{\mathcal{L}_u}(\tilde{\boldsymbol{f}}_{\boldsymbol{u}'}(\boldsymbol{v}), \tilde{\boldsymbol{f}}_{\boldsymbol{u}''}(\boldsymbol{v})) \to 0, \text{ as } \mathrm{dist}_{\mathcal{L}_u}(\boldsymbol{u}', \boldsymbol{u}'') \to 0, \tag{S2.6}$$

which is the result of uniform continuity of $\tilde{\boldsymbol{f}}$ on the compact manifold $\mathcal{L}_u \times \mathcal{L}_v$. Another fact is

$$\mathrm{dist}_{\mathcal{L}_u}(\boldsymbol{u}_{t+1}, \tilde{\boldsymbol{f}}_{\boldsymbol{u}_t}(\boldsymbol{v}_\iota)) = \mathrm{dist}_{\mathcal{L}_u}(\tilde{\boldsymbol{f}}_{\boldsymbol{u}_t}(\boldsymbol{v}_t), \tilde{\boldsymbol{f}}_{\boldsymbol{u}_t}(\boldsymbol{v}_\iota)). \tag{S2.7}$$

The triangle inequality gives

$$\left|\mathrm{dist}_{\mathcal{L}_u}(\tilde{\boldsymbol{f}}_{\boldsymbol{u}_t}(\boldsymbol{v}_\iota), \tilde{\boldsymbol{f}}_{\boldsymbol{u}_t}(\boldsymbol{v}_t)) - \mathrm{dist}_{\mathcal{L}_u}(\tilde{\boldsymbol{f}}_{\boldsymbol{u}_t}(\boldsymbol{v}_t), \tilde{\boldsymbol{f}}_{\boldsymbol{u}_\iota}(\boldsymbol{v}_\iota))\right| \leqslant \mathrm{dist}_{\mathcal{L}_u}(\tilde{\boldsymbol{f}}_{\boldsymbol{u}_t}(\boldsymbol{v}_\iota), \tilde{\boldsymbol{f}}_{\boldsymbol{u}_\iota}(\boldsymbol{v}_\iota)) \tag{S2.8}$$

which, from Eq. (S2.6), approaches zero as $\mathrm{dist}_{\mathcal{L}_u}(\boldsymbol{u}_t, \boldsymbol{u}_\iota)$ tends to zero. Applying Eqs. (S2.6) and (S2.7) as well as the inequality (S2.8), we get

$$\begin{aligned}
&\left\{\boldsymbol{v}_\iota \in \mathcal{L}_v \;\middle|\; \boldsymbol{v}_\iota \in \tilde{\boldsymbol{f}}^{-1}_{\boldsymbol{u}_t}(\mathcal{O}(\boldsymbol{u}_{t+1}, \varepsilon_{\boldsymbol{u}}))\right\} \\
&\qquad = \left\{\boldsymbol{v}_\iota \in \mathcal{L}_v \;\middle|\; \mathrm{dist}_{\mathcal{L}_u}(\boldsymbol{u}_{t+1}, \tilde{\boldsymbol{f}}_{\boldsymbol{u}_t}(\boldsymbol{v}_\iota)) < \varepsilon_{\boldsymbol{u}}\right\} \\
&\qquad = \left\{\boldsymbol{v}_\iota \in \mathcal{L}_v \;\middle|\; \mathrm{dist}_{\mathcal{L}_u}(\tilde{\boldsymbol{f}}_{\boldsymbol{u}_t}(\boldsymbol{v}_t), \tilde{\boldsymbol{f}}_{\boldsymbol{u}_t}(\boldsymbol{v}_\iota)) < \varepsilon_{\boldsymbol{u}}\right\} \\
&\qquad \approx \left\{\boldsymbol{v}_\iota \in \mathcal{L}_v \;\middle|\; \mathrm{dist}_{\mathcal{L}_u}(\tilde{\boldsymbol{f}}_{\boldsymbol{u}_t}(\boldsymbol{v}_t), \tilde{\boldsymbol{f}}_{\boldsymbol{u}_\iota}(\boldsymbol{v}_\iota)) < \varepsilon_{\boldsymbol{u}}\right\} \\
&\qquad = \left\{\boldsymbol{v}_\iota \in \mathcal{L}_v \;\middle|\; \mathrm{dist}_{\mathcal{L}_u}(\boldsymbol{u}_{t+1}, \boldsymbol{u}_{\iota+1}) < \varepsilon_{\boldsymbol{u}}\right\},
\end{aligned} \tag{S2.9}$$

provided that $\mathrm{dist}_{\mathcal{L}_u}(\boldsymbol{u}_t, \boldsymbol{u}_\iota)$ is sufficiently small. Letting $\iota = \tau - 1$ yields a new setting for the radius estimation as

$$\delta^t_{\boldsymbol{v}}(\varepsilon_{\boldsymbol{u}}) \triangleq \left\{\#[\bar{I}^t_{\boldsymbol{u}}(\varepsilon_{\boldsymbol{u}})]\right\}^{-1} \sum_{\tau \in \bar{I}^t_{\boldsymbol{u}}(\varepsilon_{\boldsymbol{u}})} \mathrm{dist}_{\mathcal{L}_v}(\boldsymbol{v}_t, \boldsymbol{v}_{\tau-1}), \tag{S2.10}$$

where

$$\bar{I}^t_{\boldsymbol{u}}(\varepsilon_{\boldsymbol{u}}) \triangleq \left\{\tau \in \mathbb{N} \;\middle|\; \mathrm{dist}_{\mathcal{L}_u}(\boldsymbol{u}_t, \boldsymbol{u}_{\tau-1}) < \varepsilon_{\boldsymbol{u}},\ \mathrm{dist}_{\mathcal{L}_u}(\boldsymbol{u}_{t+1}, \boldsymbol{u}_\tau) < \varepsilon_{\boldsymbol{u}}\right\} \tag{S2.11}$$

has been used to approximate the set $\hat{I}^t_{\boldsymbol{u}}(\varepsilon_{\boldsymbol{u}})$ specified in Eq. (S2.5). This indicates that the scaling relation at time t between $\delta^t_{\boldsymbol{v}}(\varepsilon_{\boldsymbol{u}})$ and $\ln \varepsilon_{\boldsymbol{u}}$, which describes the changes of the set $\tilde{\boldsymbol{f}}^{-1}_{\boldsymbol{u}_t}\left(\mathcal{O}(\boldsymbol{u}_{t+1}, \varepsilon_{\boldsymbol{u}}) \cap \{\boldsymbol{u}_\tau; \mathrm{dist}_{\mathcal{L}_u}(\boldsymbol{u}_t, \boldsymbol{u}_{\tau-1}) < \varepsilon_{\boldsymbol{u}}\}\right)$ with the contraction of the set $\mathcal{O}(\boldsymbol{u}_{t+1}, \varepsilon_{\boldsymbol{u}}) \cap \{\boldsymbol{u}_\tau; \mathrm{dist}_{\mathcal{L}_u}(\boldsymbol{u}_t, \boldsymbol{u}_{\tau-1}) < \varepsilon_{\boldsymbol{u}}\}$, measures the instantaneous causation from $\boldsymbol{v}$ to $\boldsymbol{u}$ at time t. When $\boldsymbol{u}$ and $\boldsymbol{v}$ are substituted, respectively, by $\boldsymbol{x}$ and $\boldsymbol{y}$, the quantity set in (S2.10) reduces to the quantity in Eq. (2) in the main text.

If the following condition is assumed,

$$\mathrm{dist}_{\mathcal{L}_u}(\boldsymbol{u}_{t+1}, \boldsymbol{u}_\tau) \to 0 \text{ implies } \mathrm{dist}_{\mathcal{L}_u}(\boldsymbol{u}_t, \boldsymbol{u}_{\tau-1}) \to 0, \quad \text{[DD]}$$

the index set $\bar{I}^t_{\boldsymbol{u}}(\varepsilon_{\boldsymbol{u}})$ as defined in (S2.11) can be further simplified as:

$$I^t_{\boldsymbol{u}}(\varepsilon_{\boldsymbol{u}}) \triangleq \left\{\tau \in \mathbb{N} \;\middle|\; \mathrm{dist}_{\mathcal{L}_u}(\boldsymbol{u}_{t+1}, \boldsymbol{u}_\tau) < \varepsilon_{\boldsymbol{u}}\right\}. \tag{S2.12}$$

Consequently, the estimation of the radius of the neighborhood becomes

$$\delta^t_{\boldsymbol{v}}(\varepsilon_{\boldsymbol{u}}) \triangleq \left\{\#[I^t_{\boldsymbol{u}}(\varepsilon_{\boldsymbol{u}})]\right\}^{-1} \sum_{\tau \in I^t_{\boldsymbol{u}}(\varepsilon_{\boldsymbol{u}})} \mathrm{dist}_{\mathcal{L}_v}(\boldsymbol{v}_t, \boldsymbol{v}_{\tau-1}). \tag{S2.13}$$

Since the scaling relation at time t between $\delta^t_{\boldsymbol{v}}(\varepsilon_{\boldsymbol{u}})$ and $\ln \varepsilon_{\boldsymbol{u}}$ is calculated for the situation where $\varepsilon_{\boldsymbol{u}}$ is close to 0, estimation (S2.13) with the simplified index set (S2.12) is applicable to the case where Condition [DD] is fulfilled. In applications, Condition [DD] is often warranted when delayed coordinates are used to reconstruct the states from the observational time series. The examples and simulations shown in Fig. S1 demonstrate the universality of Condition [DD].

The scaling relation, computed by either (S2.10) or (S2.13), represents a characterization at one time instant. To quantify the causation from $\boldsymbol{v}$ to $\boldsymbol{u}$ on the whole manifolds, we use the slope of the regression line obtained from the scaling relation between the averaged $\langle \delta^t_{\boldsymbol{v}}(\varepsilon_{\boldsymbol{u}}) \rangle_{t \in \mathbb{N}}$ and $\ln \varepsilon_{\boldsymbol{u}}$.

The scaling relation between $\langle \delta^t_{\boldsymbol{v}}(\varepsilon_{\boldsymbol{u}}) \rangle_{t \in \mathbb{N}}$ and $\ln \varepsilon_{\boldsymbol{u}}$ can also be analytically demonstrated as the following reasonings, which represents consistency with the numerical simulations. Here we consider the reconstructed system (S2.2). For any given $\varepsilon_{\boldsymbol{u}} > 0$, any $\boldsymbol{u}^* \in \mathcal{O}(\boldsymbol{u}_{t+1}, \varepsilon_{\boldsymbol{u}})$, and $\boldsymbol{v}^*$ close to $\boldsymbol{v}_t$, the Taylor expansion of $\tilde{\boldsymbol{f}}$ to the first order gives

$$\begin{aligned} \boldsymbol{u}_{t+1} - \boldsymbol{u}^* &= \tilde{\boldsymbol{f}}(\boldsymbol{u}_t, \boldsymbol{v}_t) - \boldsymbol{u}^* \\ &\approx \tilde{\boldsymbol{f}}(\boldsymbol{u}_t, \boldsymbol{v}^*) - \boldsymbol{u}^* + \frac{\partial \tilde{\boldsymbol{f}}}{\partial \boldsymbol{v}}(\boldsymbol{u}_t, \boldsymbol{v}^*)(\boldsymbol{v}_t - \boldsymbol{v}^*). \end{aligned} \tag{S2.14}$$

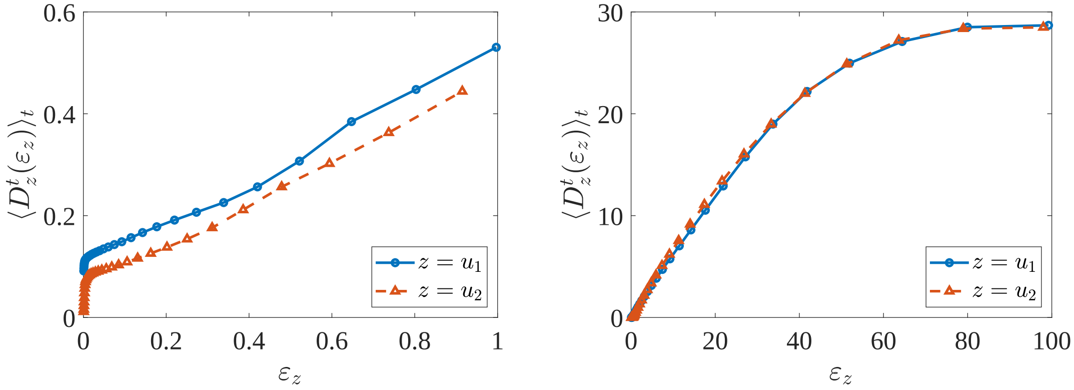

(a) (b)

FIG. S1. Two examples demonstrating the universality of Condition [DD]: $\mathrm{dist}(\boldsymbol{z}_{t+1}, \boldsymbol{z}_\tau) \rightarrow 0$ implies $\mathrm{dist}(\boldsymbol{z}_t, \boldsymbol{z}_{\tau-1}) \rightarrow 0$. The notation $\mathrm{dist}(\cdot, \cdot)$ stands for the Euclidean distance in the underlying space and $\boldsymbol{z}$ represents the relevant variable. For a given $\varepsilon_{\boldsymbol{z}} > 0$, Condition [DD] is verified through estimating the average value defined by $D^t_{\boldsymbol{z}}(\varepsilon_{\boldsymbol{z}}) \triangleq (\#[J^t_{\boldsymbol{z}}(\varepsilon_{\boldsymbol{z}})])^{-1} \sum_{\tau \in J^t_{\boldsymbol{z}}(\varepsilon_{\boldsymbol{z}})} \mathrm{dist}(\boldsymbol{z}_t, \boldsymbol{z}_{\tau-1})$, where the index set satisfies $J^t_{\boldsymbol{z}}(\varepsilon_{\boldsymbol{z}}) \triangleq \{\tau \in \mathbb{N} \mid \mathrm{dist}(\boldsymbol{z}_{t+1},\ \boldsymbol{z}_\tau) < \varepsilon_{\boldsymbol{z}},\ |t+1-\tau| > E\}$, and E is a positive threshold to avoid the situation where the nearest neighboring points are induced only by the consecutive time order. In numerical simulations, $\varepsilon_{\boldsymbol{z}}$ alters its value successively from the set $\{\varepsilon_{\boldsymbol{z},j}\}_{j=1,\cdots,N_\varepsilon}$, where $\varepsilon_{\boldsymbol{z},1} = eD_z$, $\varepsilon_{\boldsymbol{z},N_\epsilon} = D_z$ and $(\ln \varepsilon_{\boldsymbol{z},j} - \ln \varepsilon_{\boldsymbol{z},1})/(j-1) = (\ln \varepsilon_{\boldsymbol{z},N_\varepsilon} - \ln \varepsilon_{\boldsymbol{z},1})/(N_\varepsilon - 1)$, $j = 2, \ldots, N_\varepsilon - 1$. Parameter values are $N_\varepsilon = 33$, $e = 0.001$, and D_z, analogous to Eq. (2) in the main text, is the largest diameter estimated for the underlying manifold. **(a)** The two-species, unidirectionally coupled ecological system (S3.1) with $(r_1, r_2) = (3.8, 3.7)$ and the coupling coefficients $\mu_{21} = 0.05$ and $\mu_{12} = 0$. The system generates time series of 5400 points, where the first 400 points are abandoned to get rid of the transient behavior. The observational functions are $u_i(x_i) = x_i$ and the embedding parameters are $d_i = 3$ and $\tau_i = 1$ so that $\boldsymbol{u}_{i,t} = (u_{i,t}, u_{i,t+1}, u_{i,t+2})$ for $i = 1, 2$, $\boldsymbol{z} = \boldsymbol{u}_{1,2}$, and $E = 0$. **(b)** Unidirectionally coupled Lorenz system (S3.3) with $(\sigma_1, \rho_1, \beta_1) = (10.010, 27.944, 2.667)$, $(\sigma_2, \rho_2, \beta_2) = (9.990, 28.056, 2.667)$, $\mu_{21} = 4$, and $\mu_{12} = 0$. Using the Euler scheme with step size 0.001 produces time series of duration 150, in which the data points from time instant 51 to 150 are used in the analysis. The observational functions are $u_i(x_i, y_i, z_i) = y_i$. The embedding parameters are $d_i = 7$ and $\tau_i = 2\omega$, where $i = 1, 2$, $\omega = 0.016$ is the sampling duration, $\boldsymbol{z} = \boldsymbol{u}_{1,2}$, and $E = 8$. It is clear that Condition [DD] holds from the trends in (a) and (b).

Therefore,

$$\begin{aligned}
\ln\|\boldsymbol{u}_{t+1}-\boldsymbol{u}^*\| &\approx \ln\left\|\tilde{\boldsymbol{f}}(\boldsymbol{u}_t,\boldsymbol{v}^*)-\boldsymbol{u}^*+\frac{\partial\tilde{\boldsymbol{f}}}{\partial\boldsymbol{v}}(\boldsymbol{u}_t,\boldsymbol{v}^*)(\boldsymbol{v}_t-\boldsymbol{v}^*)\right\| \\
&= \frac{1}{2}\ln\left\|\tilde{\boldsymbol{f}}(\boldsymbol{u}_t,\boldsymbol{v}^*)-\boldsymbol{u}^*+\frac{\partial\tilde{\boldsymbol{f}}}{\partial\boldsymbol{v}}(\boldsymbol{u}_t,\boldsymbol{v}^*)(\boldsymbol{v}_t-\boldsymbol{v}^*)\right\|^2 \\
&= \frac{1}{2}\ln\left\{\left\|\tilde{\boldsymbol{f}}(\boldsymbol{u}_t,\boldsymbol{v}^*)-\boldsymbol{u}^*\right\|^2+2\left[\tilde{\boldsymbol{f}}(\boldsymbol{u}_t,\boldsymbol{v}^*)-\boldsymbol{u}^*\right]\right. \\
&\qquad\left.\cdot\left[\frac{\partial\tilde{\boldsymbol{f}}}{\partial\boldsymbol{v}}(\boldsymbol{u}_t,\boldsymbol{v}^*)(\boldsymbol{v}_t-\boldsymbol{v}^*)\right]+\left\|\frac{\partial\tilde{\boldsymbol{f}}}{\partial\boldsymbol{v}}(\boldsymbol{u}_t,\boldsymbol{v}^*)(\boldsymbol{v}_t-\boldsymbol{v}^*)\right\|^2\right\} \\
&\approx \frac{1}{2}\ln\left\{1+\frac{\left\|\tilde{\boldsymbol{f}}(\boldsymbol{u}_t,\boldsymbol{v}^*)-\boldsymbol{u}^*\right\|\left\|\frac{\partial\tilde{\boldsymbol{f}}}{\partial\boldsymbol{v}}(\boldsymbol{u}_t,\boldsymbol{v}^*)(\boldsymbol{v}_t-\boldsymbol{v}^*)\right\|\gamma_t}{\frac{1}{2}\left\|\tilde{\boldsymbol{f}}(\boldsymbol{u}_t,\boldsymbol{v}^*)-\boldsymbol{u}^*\right\|^2}\right\} \\
&\quad+\frac{1}{2}\ln\left(\left\|\tilde{\boldsymbol{f}}(\boldsymbol{u}_t,\boldsymbol{v}^*)-\boldsymbol{u}^*\right\|^2\right) \\
&\approx \frac{\left\|\tilde{\boldsymbol{f}}(\boldsymbol{u}_t,\boldsymbol{v}^*)-\boldsymbol{u}^*\right\|\cdot\left\|\frac{\partial\tilde{\boldsymbol{f}}}{\partial\boldsymbol{v}}(\boldsymbol{u}_t,\boldsymbol{v}^*)(\boldsymbol{v}_t-\boldsymbol{v}^*)\right\|\cdot\gamma_t}{\left\|\tilde{\boldsymbol{f}}(\boldsymbol{u}_t,\boldsymbol{v}^*)-\boldsymbol{u}^*\right\|^2} \\
&\quad+\frac{1}{2}\ln\left(\left\|\tilde{\boldsymbol{f}}(\boldsymbol{u}_t,\boldsymbol{v}^*)-\boldsymbol{u}^*\right\|^2\right) \\
&\approx \frac{\left\|\tilde{\boldsymbol{f}}(\boldsymbol{u}_t,\boldsymbol{v}^*)-\boldsymbol{u}^*\right\|\cdot\left\|\frac{\partial\tilde{\boldsymbol{f}}}{\partial\boldsymbol{v}}(\boldsymbol{u}_t,\boldsymbol{v}^*)\right\|\cdot\gamma_t}{\left\|\tilde{\boldsymbol{f}}(\boldsymbol{u}_t,\boldsymbol{v}^*)-\boldsymbol{u}^*\right\|^2}\|\boldsymbol{v}_t-\boldsymbol{v}^*\| \\
&\quad+\ln\left\|\tilde{\boldsymbol{f}}(\boldsymbol{u}_t,\boldsymbol{v}^*)-\boldsymbol{u}^*\right\|,
\end{aligned}\tag{S2.15}$$

where γ_t denotes the cosine of the angle between vectors $\tilde{\boldsymbol{f}}(\boldsymbol{u}_t,\boldsymbol{v}^*)-\boldsymbol{u}^*$ and $\frac{\partial\tilde{\boldsymbol{f}}}{\partial\boldsymbol{v}}(\boldsymbol{u}_t,\boldsymbol{v}^*)(\boldsymbol{v}_t-\boldsymbol{v}^*)$. By replacing $\|\boldsymbol{u}_{t+1}-\boldsymbol{u}^*\|$ with $\varepsilon_{\boldsymbol{u}}$ and $\|\boldsymbol{v}_t-\boldsymbol{v}^*\|$ with $\delta^t_{\boldsymbol{v}}$, we obtain

$$\ln(\varepsilon_{\boldsymbol{u}})\approx\tilde{K}^t_{\boldsymbol{v}\hookrightarrow\boldsymbol{u}}\delta^t_{\boldsymbol{v}}+\tilde{B}^t_{\boldsymbol{v}\hookrightarrow\boldsymbol{u}}\tag{S2.16}$$

with the parameters abbreviated as $\tilde{K}^t_{\boldsymbol{v}\hookrightarrow\boldsymbol{u}}$ and $\tilde{B}^t_{\boldsymbol{v}\hookrightarrow\boldsymbol{u}}$. Because $\varepsilon_{\boldsymbol{u}}$ is independent of time t, reformulating this equation (subtract $\tilde{B}^t_{\boldsymbol{v}\hookrightarrow\boldsymbol{u}}$ and then divided by $\tilde{K}^t_{\boldsymbol{v}\hookrightarrow\boldsymbol{u}}$ at both sides of (S2.16)) and taking average over time admit

$$\langle\delta^t_{\boldsymbol{v}}\rangle_t\approx\langle K^t_{\boldsymbol{v}\hookrightarrow\boldsymbol{u}}\rangle_t\ln(\varepsilon_{\boldsymbol{u}})+\langle B^t_{\boldsymbol{v}\hookrightarrow\boldsymbol{u}}\rangle_t,\tag{S2.17}$$

which clearly demonstrates the linear scaling relation. Notice that this scaling relation can be further rewritten by substituting the average over time by the average over space based on ergodic theory, i.e.,

$$\int\delta_{\boldsymbol{v}}\,\mathrm{d}\mu_{\mathcal{L}_u\times\mathcal{L}_v}\approx\int K_{\boldsymbol{v}\hookrightarrow\boldsymbol{u}}\,\mathrm{d}\mu_{\mathcal{L}_u\times\mathcal{L}_v}\ln(\varepsilon_{\boldsymbol{u}})+\int B_{\boldsymbol{v}\hookrightarrow\boldsymbol{u}}\,\mathrm{d}\mu_{\mathcal{L}_u\times\mathcal{L}_v},\tag{S2.18}$$

where $\mu_{\mathcal{L}_u\times\mathcal{L}_v}$ represents the Sinai-Ruelle-Bowen (SRB) measure [1] on $\mathcal{L}_u\times\mathcal{L}_v$.

III. ADDITIONAL EXAMPLES DEMONSTRATING THE POWER OF CONTINUITY SCALING FRAMEWORK IN ASCERTAINING AND QUANTIFYING CAUSATION

A. Unidirectionally and bidirectionally coupled systems

1. *Coupled ecological models*

The coupled map system is written as

$$x_{i,t+1} = x_{i,t}\left(r_i - r_i x_{i,t} - \sum_{j\neq i} \mu_{ij} x_{j,t}\right), \tag{S3.1}$$

where $i = 1, \ldots, N_V,\ t \in \mathbb{N}$. We consider two-species models here: $N_V = 2$ with $(r_1, r_2) = (3.8, 3.7)$ and choose different pairs of the coupling parameters $\{\mu_{ij}\}$. Time series of 5400 points are generated with the first 400 points abandoned to get rid of the transient behavior. The observational functions are $u_i(x_i) = x_i$ and the embedding parameters are $d_i = 3$ and $\tau_i = 1$ for $i = 1, 2$, and $E = 0$. In order to detect the causal relation $x_1 \hookrightarrow x_2$, we calculate the scaling relation between $\langle \delta^t_{\boldsymbol{u}_j}(\varepsilon_{\boldsymbol{u}_i})\rangle_{t\in\mathbb{N}}$ and $\ln \varepsilon_{\boldsymbol{u}_i}$ for $i, j = 1, 2$ with $i \neq j$, where $\boldsymbol{u_i}$ is the reconstructed state space vector from the observational time series $\{u_i(x_{i,t})\}_{t\in\mathbb{N}}$. In each case, the p-value is calculated with 25 random surrogates.

Case a: For the unidirectionally coupled two-species model, the scaling relations for different pairs of the coupling parameters have been shown in Figs. 3(a)-3(b) in the main text. The calculated slopes together with their p-values are listed in Tab. S2. The results validate our continuity scaling framework. Moreover, statistical fluctuation tests are performed with parameters $\mu_{12} = 0, \mu_{21} = 0.1$ and 400 uniformly generated grid initial values from $[0, 1] \times [0, 1]$. The CS results are presented in Fig. S2, showing high statistical robustness.

TABLE S2. Estimated slopes of the regression lines of the scaling relations and their p-values for the unidirectionally coupled ecological models.

No.	$s_{\boldsymbol{u}_1\hookrightarrow\boldsymbol{u}_2}$	$s_{\boldsymbol{u}_2\hookrightarrow\boldsymbol{u}_1}$	μ_{21}	μ_{12}	p-value ($s_{\boldsymbol{u}_1\hookrightarrow\boldsymbol{u}_2}$)	p-value ($s_{\boldsymbol{u}_2\hookrightarrow\boldsymbol{u}_1}$)
1	0.0004	0.0005	0.00	0.00	0.2680	0.1641
2	0.1167	-0.0002	0.05	0.00	0.0000	0.8385
3	0.1203	0.0006	0.10	0.00	0.0000	0.7673
4	0.1238	0.0005	0.15	0.00	0.0000	0.3864

Case b: For the bidirectionally coupled two-species model, the scaling relations for different parameter combinations are shown in Fig. S3. The slopes with their p-values are listed in Tab. S3, also providing validation to the continuity scaling framework. Statistical fluctuation tests showing high robustness of the CS framework are shown in Fig. S4.

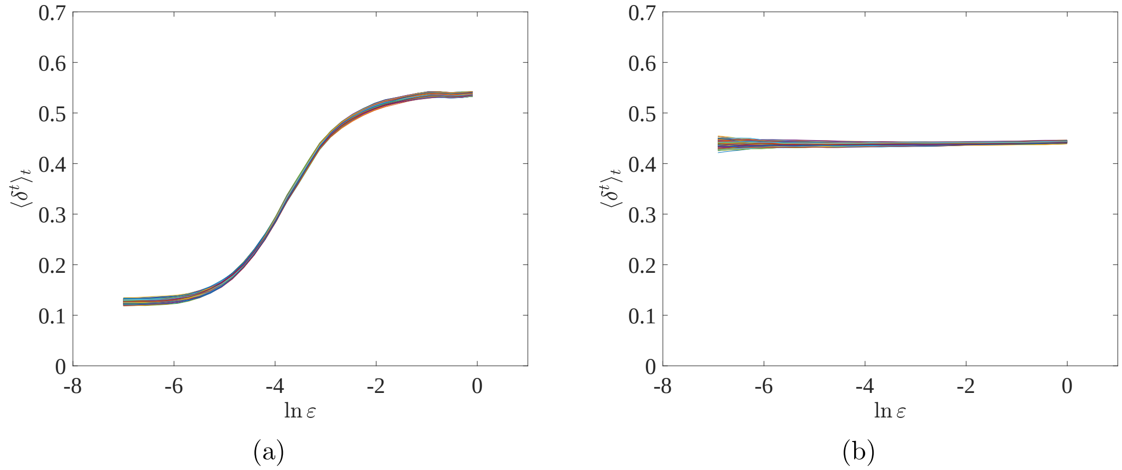

FIG. S2. Statistical fluctuation tests with the unidirectionally coupled two-species models (S3.1). Results for $\mu_{12} = 0$ and $\mu_{21} = 0.1$ and 400 grid initial values from $[0,1] \times [0,1]$ are shown. (a) The scaling relation for detecting the causation $x_1 \hookrightarrow x_2$ with mean CS index value 0.1240 and standard deviation 0.0015. (b) The scaling relation for detecting the causation $x_2 \hookrightarrow x_1$ with mean CS index value 0.0006 and standard deviation 0.0006.

Case c: For the unidirectionally coupled two-species model subject to noise:

$$x_{i,t+1} = x_{i,t}\left(r_i - r_i x_{i,t} - \sum_{j\neq i} \mu_{ij} x_{j,t}\right) + U_{i,t}, \quad i = 1, 2, \tag{S3.2}$$

where $\{U_{1,t}, U_{2,t}\}_{\mathbb{N}}$ are i.i.d. random variables uniformly distributed on $[-\sigma, \sigma]$ and $\mu_{21} = 0.1$, the representative scaling relations are shown in Fig. S5 and the estimated slopes with their p-values are listed in Tab. S4, demonstrating good robustness of our framework against noise.

TABLE S3. Estimated slopes of the regression lines associated with the scaling relations in Fig. S3 and their p-values for the bidirectionally coupled two-species model.

No.	$s_{\boldsymbol{u}_1 \hookrightarrow \boldsymbol{u}_2}$	$s_{\boldsymbol{u}_2 \hookrightarrow \boldsymbol{u}_1}$	μ_{21}	μ_{12}	p-value ($s_{\boldsymbol{u}_1 \hookrightarrow \boldsymbol{u}_2}$)	p-value ($s_{\boldsymbol{u}_2 \hookrightarrow \boldsymbol{u}_1}$)
1	0.0007	0.0929	0.00	0.05	0.1555	0.0000
2	0.1092	0.0986	0.05	0.05	0.0000	0.0000
3	0.1183	0.0976	0.10	0.05	0.0000	0.0000
4	0.1217	0.0937	0.15	0.05	0.0000	0.0000

2. Coupled Lorenz systems

The system equations are

$$\begin{aligned} \dot{x}_{i,t} &= \sigma_i(y_{i,t} - x_{i,t}) + \textstyle\sum_{j\neq i} \mu_{ij} x_{j,t}, \\ \dot{y}_{i,t} &= x_{i,t}(\rho_i - z_{i,t}) - y_{i,t}, \\ \dot{z}_{i,t} &= x_{i,t} y_{i,t} - \beta_i z_{i,t}, \end{aligned} \tag{S3.3}$$

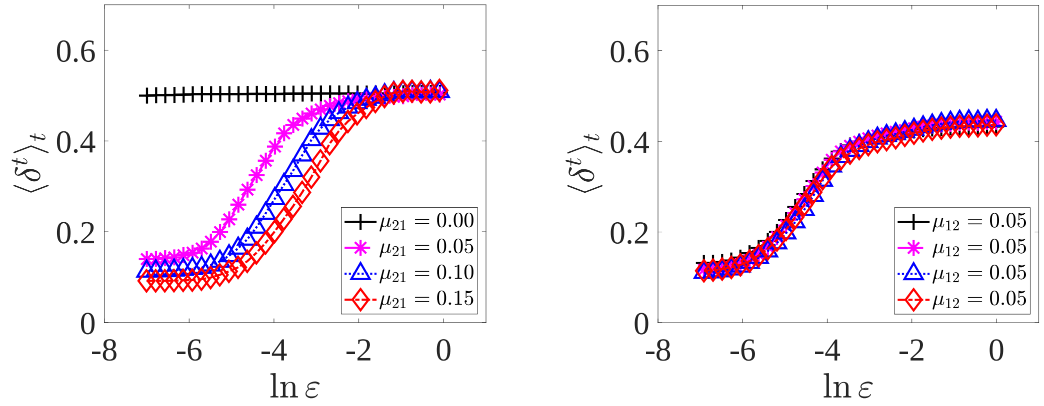

(a) (b)

FIG. S3. Detecting causation in the bidirectionally coupled two-species models (S3.1). Results for fixed $\mu_{12} = 0.05$ and a number of μ_{21} values are shown. (a) The scaling relation between $\langle \delta^t_{\boldsymbol{u}_1}(\varepsilon_{\boldsymbol{u}_2})\rangle_t$ and $\ln \varepsilon_{\boldsymbol{u}_2}$ for detecting the causation $x_1 \hookrightarrow x_2$. (b) The scaling relation between $\langle \delta^t_{\boldsymbol{u}_2}(\varepsilon_{\boldsymbol{u}_1})\rangle_t$ and $\ln \varepsilon_{\boldsymbol{u}_1}$ for detecting the causation $x_2 \hookrightarrow x_1$.

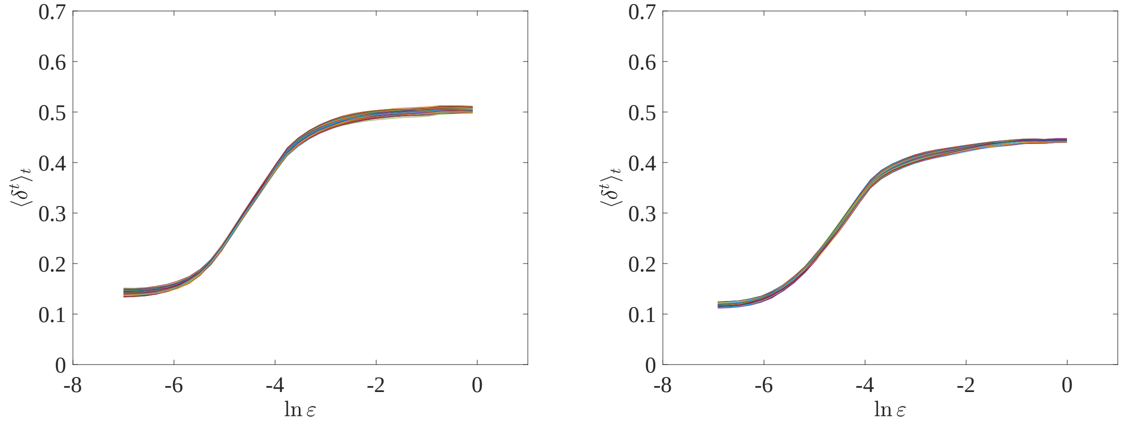

(a) (b)

FIG. S4. Statistical fluctuation tests with the bidirectionally coupled two-species models (S3.1). Results for $\mu_{12} = 0.05$ and $\mu_{21} = 0.05$ and 400 grid initial values from $[0, 1] \times [0, 1]$ are shown. (a) The scaling relation for detecting the causation $x_1 \hookrightarrow x_2$ with mean CS index value 0.1123 and standard deviation 0.0016. (b) The scaling relation for detecting the causation $x_2 \hookrightarrow x_1$ with mean CS index value 0.0975 and standard deviation 0.0014.

where $i = 1, \ldots, N_V,\ t \in \mathbb{R}$. Here we set $N_V = 2$, $(\sigma_1, \rho_1, \beta_1) = (10.010, 27.944, 2.667)$, and $(\sigma_2, \rho_2, \beta_2) = (9.990, 28.056, 2.667)$. Different combinations of the coupling parameters are used to validate the continuity scaling framework for this continuous-time dynamical system. Euler scheme is used with step size 0.001 to produce time series of duration 150 and the data points from time instant 51 to 150 are used in the analysis. The observational functions are $u_i(x_i, y_i, z_i) = y_i$. The embedding parameters are $d_i = 7$ and $\tau_i = 2\omega$, where $i = 1, 2$. Sampling duration $\omega = 0.016$, and $E = 8$. Each p-value is calculated with 20 random surrogates.

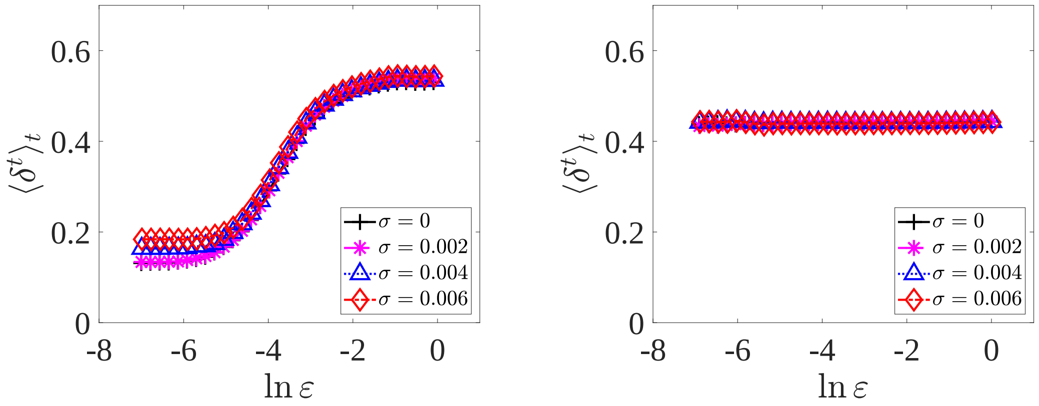

(a) (b)

FIG. S5. Detecting causation in the unidirectionally coupled two-species system (S3.2) under noise perturbation. The fixed parameters are $\mu_{12} = 0$ and $\mu_{21} = 0.1$. The noise amplitude σ varies as indicated inside each panel. (a) The scaling relation between $\langle\delta^t_{\boldsymbol{u}_1}(\varepsilon_{\boldsymbol{u}_2})\rangle_t$ and $\ln\varepsilon_{\boldsymbol{u}_2}$ for detecting the causal relation $x_1 \hookrightarrow x_2$. (b) The scaling relation between $\langle\delta^t_{\boldsymbol{u}_2}(\varepsilon_{\boldsymbol{u}_1})\rangle_t$ and $\ln\varepsilon_{\boldsymbol{u}_1}$ nullifying the causal relation $x_2 \hookrightarrow x_1$.

TABLE S4. Estimated slopes of the regression lines associated with the scaling relations in Fig. S5 and their p-values for the unidirectionally coupled two-species model for different values of the noise amplitude.

No.	$s_{\boldsymbol{u}_1\hookrightarrow\boldsymbol{u}_2}$	$s_{\boldsymbol{u}_2\hookrightarrow\boldsymbol{u}_1}$	σ	p-value ($s_{\boldsymbol{u}_1\hookrightarrow\boldsymbol{u}_2}$)	p-value ($s_{\boldsymbol{u}_2\hookrightarrow\boldsymbol{u}_1}$)
1	0.1203	0.0006	0.000	0.0000	0.1637
2	0.1203	0.0011	0.002	0.0000	0.9373
3	0.1149	-0.0000	0.004	0.0000	0.5167
4	0.1131	-0.0001	0.006	0.0000	0.2990

Case d: For the unidirectionally coupled Lorenz system, the continuity scaling relations are shown in Fig. S6 with the slopes and their p-values listed in Tab. S5. Moreover, statistical fluctuation tests are performed with parameters $\mu_{12} = 0, \mu_{21} = 3$ and 400 randomly generated initial values from $[-3,3] \times [-3,3] \times [-3,3]$. The CS results are presented in Fig. S7, showing high statistical robustness.

Case e: For the bidirectionally coupled Lorenz system, the scaling relations are shown in Fig. S8 with the slopes and their p-values listed in Tab. S6. Statistical fluctuation tests showing high robustness of the CS framework are shown in Fig. S9.

Case f: The unidirectionally coupled Lorenz system with noise perturbation is given by

$$\begin{aligned} \mathrm{d}x_{i,t} &= \left(\sigma_i(y_{i,t}-x_{i,t})+\textstyle\sum_{j\neq i}\mu_{ij}x_{j,t}\right)\mathrm{d}t+\sigma\cdot\mathrm{d}W_{i,x,t}, \\ \mathrm{d}y_{i,t} &= (x_{i,t}(\rho_i-z_{i,t})-y_{i,t})\mathrm{d}t+\sigma\cdot\mathrm{d}W_{i,y,t}, \\ \mathrm{d}z_{i,t} &= (x_{i,t}y_{i,t}-\beta_i z_{i,t})\mathrm{d}t+\sigma\cdot\mathrm{d}W_{i,z,t}, \end{aligned} \tag{S3.4}$$

where $i=1,2,\ t\in\mathbb{R}$ and each $W_i=\{(W_{i,x,t},W_{i,y,t},W_{i,z,t})\}_t$ is a standard Wiener process of dimension three, $W_{1,2}$ are mutually independent, $\mu_{21}=4$, and σ is the noise amplitude. The scaling relations are shown in Fig. S10 with the slopes and their p-values listed in Tab. S7. Results demonstrate good robustness against noise for our continuity scaling framework.

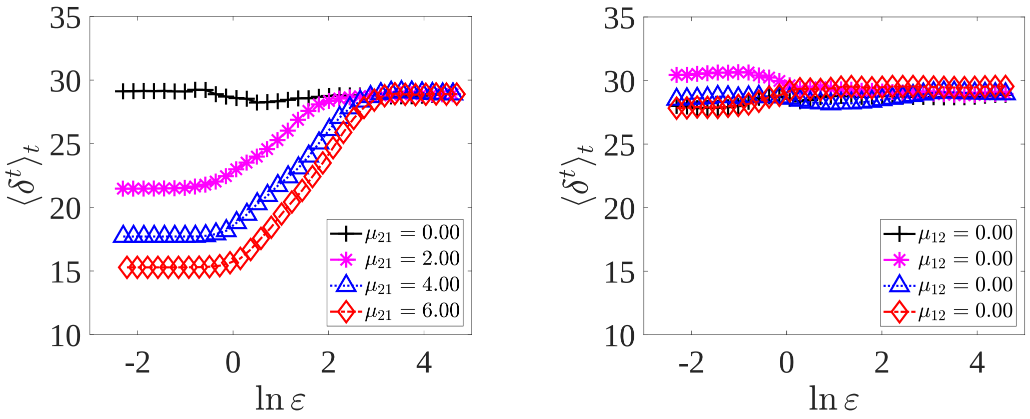

(a) (b)

FIG. S6. Causal detection in the unidirectionally coupled Lorenz system (S3.3). Various values of μ_{21} are indicated inside the left panel. (a) Scaling relation between $\langle\delta^t_{\boldsymbol{u}_1}(\varepsilon_{\boldsymbol{u}_2})\rangle_t$ and $\ln\varepsilon_{\boldsymbol{u}_2}$ for identifying the causal relation $x_1\hookrightarrow x_2$. (b) Scaling relation between $\langle\delta^t_{\boldsymbol{u}_2}(\varepsilon_{\boldsymbol{u}_1})\rangle_t$ and $\ln\varepsilon_{\boldsymbol{u}_1}$ for demonstrating nonexistence of the causal relation $x_2\hookrightarrow x_1$.

TABLE S5. Slopes of the regression lines associated with the scaling relations in Fig. S6 and their p-values for the unidirectionally coupled Lorenz system.

No.	$s_{\boldsymbol{u}_1\hookrightarrow\boldsymbol{u}_2}$	$s_{\boldsymbol{u}_2\hookrightarrow\boldsymbol{u}_1}$	μ_{21}	μ_{12}	p-value	p-value
					$(s_{\boldsymbol{u}_1\hookrightarrow\boldsymbol{u}_2})$	$(s_{\boldsymbol{u}_2\hookrightarrow\boldsymbol{u}_1})$
1	-0.0620	0.1363	0.00	0.00	0.7247	0.2292
2	2.4251	-0.2906	2.00	0.00	0.0000	0.9237
3	3.5427	0.0279	4.00	0.00	0.0000	0.6066
4	4.3265	0.2967	6.00	0.00	0.0000	0.1916

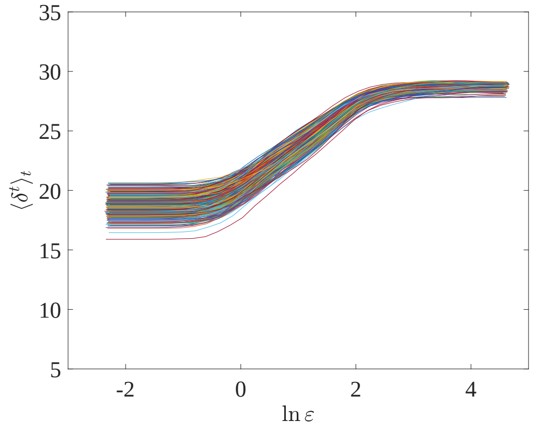

(a) (b)

FIG. S7. Statistical fluctuation tests with the unidirectionally coupled Lorenz system (S3.3). Results for $\mu_{12} = 0$ and $\mu_{21} = 3$ and 400 randomly generated initial values from $[-3, 3] \times [-3, 3] \times [-3, 3]$ are shown. (a) The scaling relation for detecting the causation $x_1 \hookrightarrow x_2$ with mean CS index value 3.1231 and standard deviation 0.2538. (b) The scaling relation for detecting the causation $x_2 \hookrightarrow x_1$ with mean CS index value 0.0575 and standard deviation 0.2004.

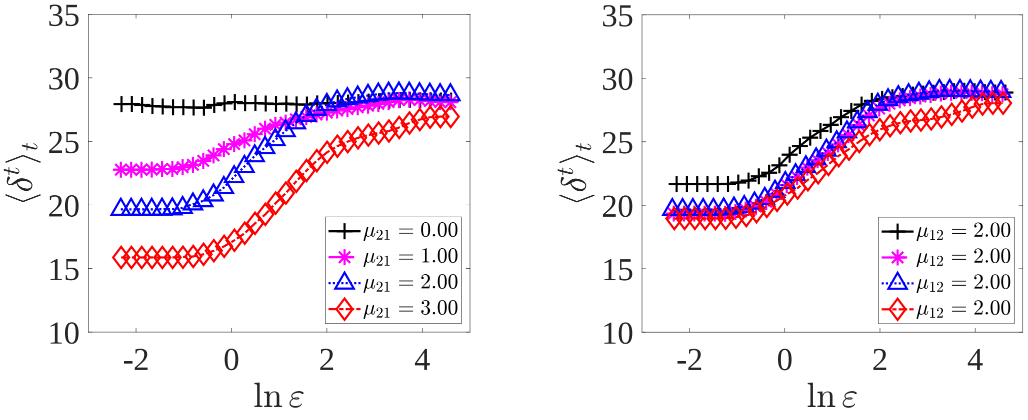

(a) (b)

FIG. S8. Detecting causation in the bidirectionally coupled Lorenz system (S3.3) for fixed $\mu_{12} = 2$. Various values of μ_{21} are indicated inside the left panel. (a) Scaling relation between $\langle \delta^t_{\boldsymbol{u}_1}(\varepsilon_{\boldsymbol{u}_2})\rangle_t$ and $\ln \varepsilon_{\boldsymbol{u}_2}$ for ascertaining the causal relation $x_1 \hookrightarrow x_2$. (b) Scaling relation between $\langle \delta^t_{\boldsymbol{u}_2}(\varepsilon_{\boldsymbol{u}_1})\rangle_t$ and $\ln \varepsilon_{\boldsymbol{u}_1}$ for confirming the causal relation $x_2 \hookrightarrow x_1$.

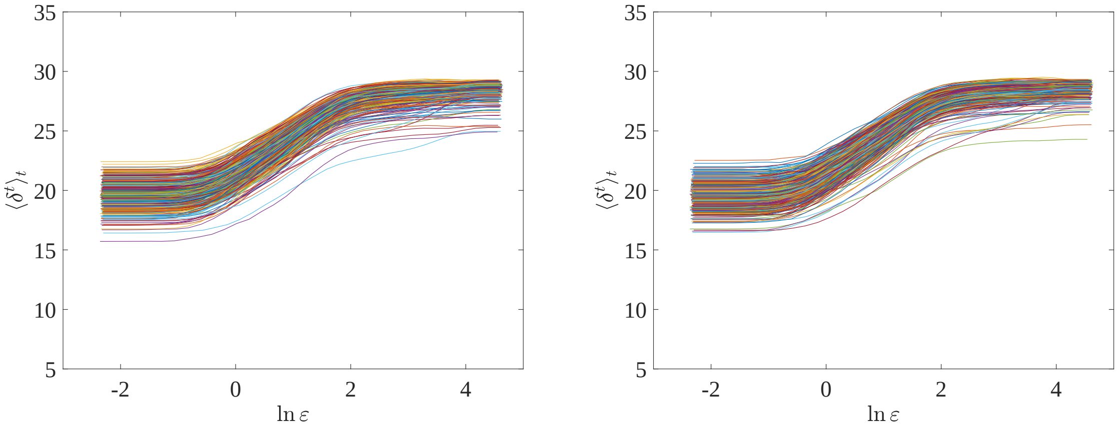

(a) (b)

FIG. S9. Statistical fluctuation tests with the bidirectionally coupled Lorenz system (S3.3). Results for $\mu_{12} = 2$ and $\mu_{21} = 2$ and 400 randomly generated initial values from $[-3,3] \times [-3,3] \times [-3,3]$ are shown. (a) The scaling relation for detecting the causation $x_1 \hookrightarrow x_2$ with mean CS index value 2.5565 and standard deviation 0.4125. (b) The scaling relation for detecting the causation $x_2 \hookrightarrow x_1$ with mean CS index value 2.5861 and standard deviation 0.4073.

TABLE S6. Slopes of the regression lines associated with the scaling relations in Fig. S8 and their p-values for the bidirectionally coupled Lorenz system.

No.	$s_{\boldsymbol{u}_1 \hookrightarrow \boldsymbol{u}_2}$	$s_{\boldsymbol{u}_2 \hookrightarrow \boldsymbol{u}_1}$	μ_{21}	μ_{12}	p-value ($s_{\boldsymbol{u}_1 \hookrightarrow \boldsymbol{u}_2}$)	p-value ($s_{\boldsymbol{u}_2 \hookrightarrow \boldsymbol{u}_1}$)
1	0.0695	2.2773	0.00	2.00	0.3754	0.0001
2	1.2333	2.8261	1.00	2.00	0.0000	0.0000
3	2.8006	2.8561	2.00	2.00	0.0000	0.0000
4	2.7493	1.9162	3.00	2.00	0.0000	0.0002

TABLE S7. Slopes of the regression lines associated with the scaling relations in Fig. S10 and their p-values for the unidirectionally coupled Lorenz system under noise perturbation of different amplitudes.

No.	$s_{\boldsymbol{u}_1 \hookrightarrow \boldsymbol{u}_2}$	$s_{\boldsymbol{u}_2 \hookrightarrow \boldsymbol{u}_1}$	σ	p-value ($s_{\boldsymbol{u}_1 \hookrightarrow \boldsymbol{u}_2}$)	p-value ($s_{\boldsymbol{u}_2 \hookrightarrow \boldsymbol{u}_1}$)
1	3.5427	0.0279	0.00	0.0000	0.6275
2	3.2192	-0.2594	0.08	0.0000	0.7441
3	3.4558	0.1312	0.16	0.0000	0.4412
4	3.1478	0.1133	0.24	0.0000	0.5063

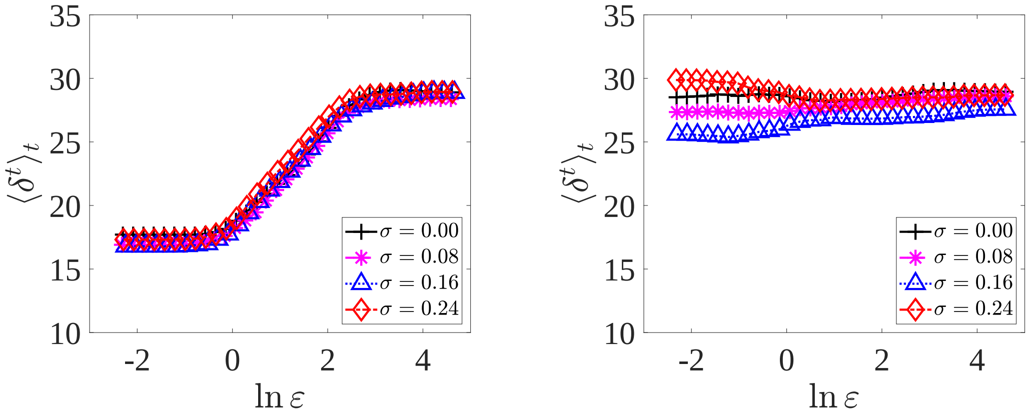

(a)

(b)

FIG. S10. Detecting causation in the unidirectionally coupled Lorenz system (S3.4) under noise perturbations. The coupling parameter values are $\mu_{12} = 0$ and $\mu_{21} = 4$. The various values of the noise amplitude σ are indicated inside each panel. (a) Scaling relation between $\langle \delta^t_{\boldsymbol{u}_1}(\varepsilon_{\boldsymbol{u}_2}) \rangle_t$ and $\ln \varepsilon_{\boldsymbol{u}_2}$ for ascertaining the causal relation $x_1 \hookrightarrow x_2$. (b) Scaling relation between $\langle \delta^t_{\boldsymbol{u}_2}(\varepsilon_{\boldsymbol{u}_1}) \rangle_t$ and $\ln \varepsilon_{\boldsymbol{u}_1}$ demonstrating nonexistence of the causal relation $x_2 \hookrightarrow x_1$.

3. Coupled Rössler-Lorenz systems

The system equations are

$$\begin{aligned}
\dot{x}_{1,t} &= -\alpha(y_{1,t} + z_{1,t}),\\
\dot{y}_{1,t} &= \alpha(x_{1,t} + 0.2 y_{1,t}),\\
\dot{z}_{1,t} &= \alpha[0.2 + z_{1,t}(x_{1,t} - 5.7)],\\
\\
\dot{x}_{2,t} &= \sigma(y_{2,t} - z_{2,t}) \; + \mu_{21} y_{1,t},\\
\dot{y}_{2,t} &= x_{2,t}(\rho - z_{2,t}) - y_{2,t},\\
\dot{z}_{2,t} &= x_{2,t} y_{2,t} - \beta z_{2,t},
\end{aligned} \tag{S3.5}$$

where $\alpha = 6$, $\sigma = 10.01$, $\rho = 28.028$, and $\beta = 2.664$. There is unidirectional coupling from the Rössler to the Lorenz system. Time series of duration 280 are generated using the Euler scheme with the step size 0.001. The data points before $t = 81$ are disregarded to eliminate transient behaviors. The observational functions are $u_1(x_1, y_1, z_1) = x_1 + 0.01 y_1 + 0.1 \sin(z_1)$ and $u_2(x_2, y_2, z_2) = y_2 - 0.01 x_2 + 0.1 \cos(z_2)$. Other parameters are: sampling duration $\omega = 0.016$, embedding dimensions $d_1 = 13$ and $d_2 = 8$, time delay $\tau_1 = 2\omega$ and $\tau_2 = 3\omega$, $E = 10$, and 20 random surrogates are used to calculate the p-value. The scaling relations are displayed in Fig. S11 and the corresponding slopes together with their p-values are listed in Tab. S8. All the results show our continuity scaling framework is highly effective in detecting causation in nonlinear dynamical systems.

B. Effects of varying sampling duration

To assess the effects of sampling duration on causation detection in continuous-time dynamical systems, we take the unidirectionally coupled Lorenz system (S3.3) with $N_V = 2$

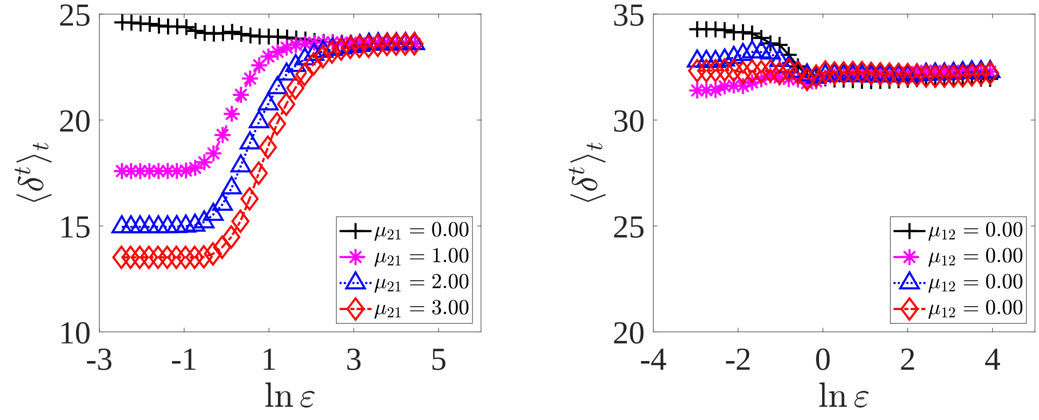

(a) (b)

FIG. S11. Detecting causation in the unidirectionally coupled Rössler-Lorenz system (S3.5). The value of the coupling parameter μ_{21} is varied systematically from $\{0, 1, 2, 3\}$, while the parameter μ_{12} is set to be zero (unidirectional coupling from the Rössler to the Lorenz system). (a) Scaling relation between $\langle\delta^t_{\boldsymbol{u}_1}(\varepsilon_{\boldsymbol{u}_2})\rangle_t$ and $\ln\varepsilon_{\boldsymbol{u}_2}$ for ascertaining the causal relation $(x_1, y_1, z_1) \hookrightarrow (x_2, y_2, z_2)$. (b) Scaling relation between $\langle\delta^t_{\boldsymbol{u}_2}(\varepsilon_{\boldsymbol{u}_1})\rangle_t$ and $\ln\varepsilon_{\boldsymbol{u}_1}$ nullifying the causal relation $(x_2, y_2, z_2) \hookrightarrow (x_1, y_1, z_1)$.

TABLE S8. Slopes of the regression lines associated with the scaling relations in Fig. S11 and their p-values for the unidirectionally coupled Rössler-Lorenz system.

No.	$s_{\boldsymbol{u}_1\hookrightarrow\boldsymbol{u}_2}$	$s_{\boldsymbol{u}_2\hookrightarrow\boldsymbol{u}_1}$	μ_{21}	μ_{12}	p-value ($s_{\boldsymbol{u}_1\hookrightarrow\boldsymbol{u}_2}$)	p-value ($s_{\boldsymbol{u}_2\hookrightarrow\boldsymbol{u}_1}$)
1	-0.1596	-0.3893	0.00	0.00	0.8617	0.9756
2	2.1836	0.1440	1.00	0.00	0.0000	0.2468
3	2.8633	-0.1323	2.00	0.00	0.0000	0.8563
4	3.4286	-0.0322	3.00	0.00	0.0000	0.7518

as an example. The simulation setting in terms of the system parameters, the observational functions, and the embedding dimension, is the same as that in section III.A.2. We conduct 60 numerical runs: for $\mu_{21} = \{0, 2, 4, 6\}$ and $\{\omega^k\}_{k=1,\cdots,15}$. The delay time $\tau = \tau^k$, the threshold $E = E^k$, and the length of the time series $L = 50 + T^k$ are used and shown in Tab. S9. The calculated slope values of the continuity scaling are shown in Fig. 4, with more details listed in Tab. S9. Notice that even with relatively low sampling rate, our continuity scaling framework can successfully detect and quantify the strength of causation.

C. Additional examples with complex nonlinear coupling schemes

In addition to the linear coupling schemes as we discussed for the coupled Lorenz system (S3.3), our continuity scaling framework is also effective for nonlinear couplings as in the coupled ecological system (S3.1). To further investigate the universality of

TABLE S9. Slopes of the regression lines associated with the continuity scaling for the unidirectionally coupled Lorenz system with different sampling durations.

	$s_{\boldsymbol{u}_1 \hookrightarrow \boldsymbol{u}_2}$				$s_{\boldsymbol{u}_2 \hookrightarrow \boldsymbol{u}_1}$							
	μ_{21}	μ_{21}	μ_{21}	μ_{21}	μ_{12}	μ_{12}	μ_{12}	μ_{12}				
k	0	2	4	6	0	0	0	0	ω^k	τ^k	E^k	T^k
1	0.200	2.349	4.519	4.375	0.234	0.205	0.041	0.275	0.004	0.048	20	60
2	0.067	3.115	4.930	4.578	0.131	0.308	0.144	0.030	0.005	0.050	20	75
3	-0.210	3.118	4.573	4.574	0.100	0.348	0.200	0.002	0.006	0.048	16	80
4	-0.209	3.966	4.164	4.751	-0.101	0.273	0.082	0.143	0.007	0.049	16	90
5	0.016	3.004	4.545	4.830	-0.172	0.009	0.169	0.189	0.008	0.048	16	100
6	-0.045	3.377	4.573	5.290	-0.073	-0.018	0.251	0.169	0.009	0.054	12	100
7	-0.073	3.139	4.305	5.004	-0.083	0.102	0.215	-0.011	0.010	0.050	12	100
8	0.028	3.467	4.624	5.366	-0.077	-0.005	0.034	0.165	0.011	0.055	12	100
9	-0.077	2.864	4.153	4.853	-0.108	-0.017	0.094	-0.035	0.012	0.048	8	100
10	-0.071	3.208	4.445	5.176	-0.213	0.282	0.171	0.077	0.013	0.052	8	100
11	0.073	2.727	3.761	4.457	-0.301	-0.002	0.138	0.056	0.014	0.042	8	100
12	-0.209	2.751	3.895	4.697	-0.032	-0.005	0.153	0.094	0.015	0.045	8	100
13	0.122	2.858	4.116	4.899	0.118	-0.285	0.306	0.089	0.016	0.048	8	100
14	-0.104	3.165	4.334	5.126	-0.039	0.036	0.260	0.319	0.017	0.051	8	100
15	0.093	3.143	4.535	5.331	0.200	0.020	0.172	0.223	0.018	0.054	8	100

continuity scaling in systems with more complex nonlinear coupling schemes, we consider the following examples. For the first example, we use the unidirectionally coupled Lorenz systems:

$$\begin{aligned}
\dot{x}_{1,t} &= \sigma_1(y_{1,t} - x_{1,t}),\\
\dot{y}_{1,t} &= x_{1,t}(\rho_1 - z_{1,t}) - y_{1,t},\\
\dot{z}_{1,t} &= x_{1,t}y_{1,t} - \beta_1 z_{1,t},\\
\\
\dot{x}_{2,t} &= \sigma_2(y_{2,t} - x_{2,t}) + \mu_{21}\Omega(x_{1,t}, y_{1,t}, z_{1,t}),\\
\dot{y}_{2,t} &= x_{2,t}(\rho_2 - z_{2,t}) - y_{2,t},\\
\dot{z}_{2,t} &= x_{2,t}y_{2,t} - \beta_2 z_{2,t}
\end{aligned} \tag{S3.6}$$

with the nonlinear coupling function $\Omega(x, y, z) = x^3/400 + 20\sin(0.1x)$. System parameters are taken as: $(\sigma_1, \rho_1, \beta_1) = (10.010, 27.944, 2.667)$ and $(\sigma_2, \rho_2, \beta_2) = (9.990, 28.056, 2.667)$. Euler scheme with time step 0.001 is used to generate the time series with a length of 150, and the points in the first time duration, 50, are discarded to eliminate the transient states. We set the sampling duration as $\omega = 0.016$, the embedding dimension and the delay time as, respectively, 7ω and 2ω, and as $e = 0.001$, $N_\varepsilon = 33$, and $E = 8$. The observational functions are supposed to be $u_i(x_i, y_i, z_i) = y_i$, $i = 1, 2$. We change the coupling parameter μ_{21} in the set $\{0, 1, 2, 3\}$ and keep $\mu_{12} = 0$ (viz. unidirectional coupling). There are 20 surrogates generated for calculating the corresponding p-values. As shown in Fig. S12 and Tab. S10, the continuity scaling is still effective even with very complex nonlinear couplings, further demonstrating the universality of our framework.

As another illustrative example with nonlinear coupling, we use the unidirectionally

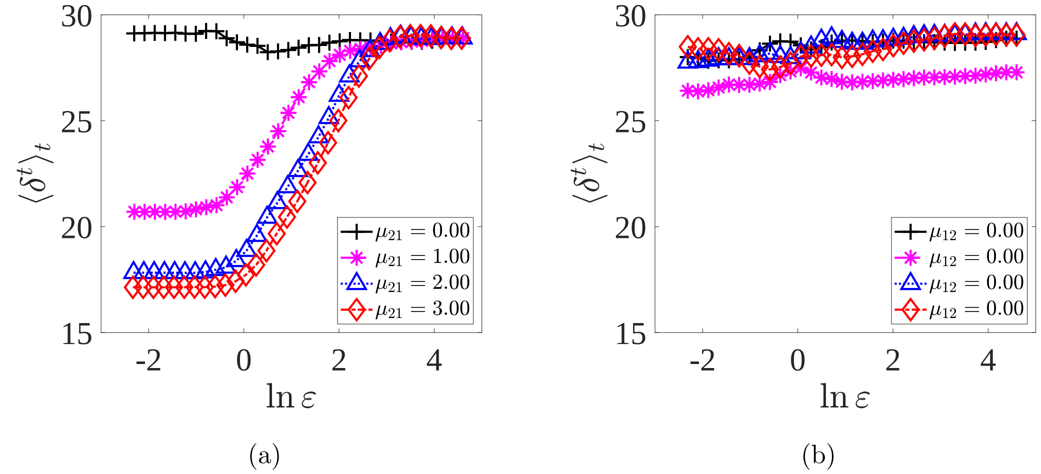

FIG. S12. Detecting causation in the unidirectionally nonlinearly coupled Lorenz system (S3.6). The value of the coupling parameter μ_{21} is varied systematically from $\{0, 1, 2, 3\}$, while the parameter μ_{12} is set to be zero. (a) Scaling relation between $\langle\delta^t_{\boldsymbol{u}_1}(\varepsilon_{\boldsymbol{u}_2})\rangle_t$ and $\ln\varepsilon_{\boldsymbol{u}_2}$ for ascertaining the causal relation $x_1 \hookrightarrow x_2$. (b) Scaling relation between $\langle\delta^t_{\boldsymbol{u}_2}(\varepsilon_{\boldsymbol{u}_1})\rangle_t$ and $\ln\varepsilon_{\boldsymbol{u}_1}$ nullifying the causal relation $x_2 \hookrightarrow x_1$.

TABLE S10. Slopes of the regression lines associated with the scaling relations in Fig. S12 and their p-values for the unidirectionally nonlinearly coupled Lorenz system.

No.	$s_{\boldsymbol{u}_1\hookrightarrow\boldsymbol{u}_2}$	$s_{\boldsymbol{u}_2\hookrightarrow\boldsymbol{u}_1}$	μ_{21}	μ_{12}	p-value ($s_{\boldsymbol{u}_1\hookrightarrow\boldsymbol{u}_2}$)	p-value ($s_{\boldsymbol{u}_2\hookrightarrow\boldsymbol{u}_1}$)
1	-0.06196	0.13625	0	0	0.6560	0.1497
2	2.28164	0.08594	1	0	0.0000	0.4996
3	3.47241	0.24354	2	0	0.0000	0.4427
4	3.77883	0.38925	3	0	0.0000	0.3290

coupled discrete-time Hénon system:

$$\begin{aligned} x_{1,t+1} &= 1 - a_1 x_{1,t}^2 + y_{1,t}, \\ y_{1,t+1} &= b_1 x_{1,t}, \\ \\ x_{2,t+1} &= 1 - a_2 x_{2,t}^2 + y_{2,t} + \mu_{21}\Omega(x_{1,t}, y_{1,t}), \\ y_{2,t+1} &= b_2 x_{2,t} \end{aligned} \tag{S3.7}$$

with the coupling function $\Omega(x, y) = \frac{2}{3}x^2 - \frac{1}{5}\sin(x)$. Time series of length 20400 are generated with the first 400 points that are discarded to eliminate the transient states. We set the sampling duration as $\omega = 4$, change the coupling strength μ_{21} in the set $\{0, 0.015, 0.030, 0.045\}$ and keep $\mu_{12} = 0$ (viz. unidirectional coupling). We set the system parameters as $[a_1, b_1] = [1.4, 0.2]$, $[a_2, b_2] = [1.401, 0.201]$ and the observational functions as $u_1(x_1, y_1) = x_1$ and $u_2(x_2, y_2) = x_2$. Additionally, we select the embedding dimension and the delay time as, respectively, 5ω and 1ω, and as $E = 0$, $e = 0.001$, and $N_\varepsilon = 33$.

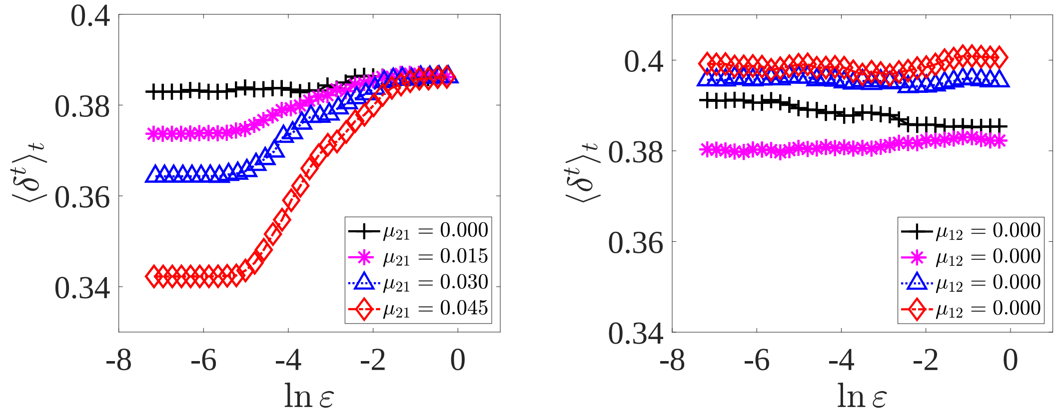

(a) (b)

FIG. S13. Detecting causation in the unidirectionally nonlinearly coupled Hénon system (S3.7). The value of the coupling parameter μ_{21} is varied systematically from $\{0, 0.015, 0.030, 0.045\}$, while the parameter μ_{12} is set to be zero. (a) Scaling relation between $\langle\delta^t_{\boldsymbol{u}_1}(\varepsilon_{\boldsymbol{u}_2})\rangle_t$ and $\ln\varepsilon_{\boldsymbol{u}_2}$ for ascertaining the causal relation $x_1 \hookrightarrow x_2$. (b) Scaling relation between $\langle\delta^t_{\boldsymbol{u}_2}(\varepsilon_{\boldsymbol{u}_1})\rangle_t$ and $\ln\varepsilon_{\boldsymbol{u}_1}$ nullifying the causal relation $x_2 \hookrightarrow x_1$.

TABLE S11. Slopes of the regression lines associated with the scaling relations in Fig. S13 and their p-values for the unidirectionally nonlinearly coupled Hénon system.

No.	$s_{\boldsymbol{u}_1\hookrightarrow\boldsymbol{u}_2}$	$s_{\boldsymbol{u}_2\hookrightarrow\boldsymbol{u}_1}$	μ_{21}	μ_{12}	p-value ($s_{\boldsymbol{u}_1\hookrightarrow\boldsymbol{u}_2}$)	p-value ($s_{\boldsymbol{u}_2\hookrightarrow\boldsymbol{u}_1}$)
1	0.000556	-0.001033	0.000	0.00	0.1210	0.9876
2	0.003331	0.000539	0.015	0.00	0.0000	0.2447
3	0.005790	-0.000204	0.030	0.00	0.0000	0.6443
4	0.012026	0.000077	0.045	0.00	0.0000	0.5384

There are 28 surrogates generated to calculate the p-values. The results presented in Fig. S13 and Tab. S11 also validate the efficacy of our framework of the continuity scaling.

In addition, to show the superior efficacy of our framework to the other existing methods in detecting causation in the form of the nonlinear couplings, we present here a comparison on the unidirectionally coupled Hénon system (S3.7) with the continuity scaling framework and the CCM technique. We depict the index values for the continuity scaling (the slope) and the CCM (see section IV) as the coupling parameter μ_{21} increasing from 0 to 0.04 and μ_{12} sustaining at zero. All the other parameters are set in the same manner as those used in the above example. Figure S14 shows a clear distinction for the directions with and without causations for the continuity scaling. However, the CCM can hardly distinguish the correct causation [see the two intertwined curves in Fig. S14(b)], even bringing reversal, wrong identifications for some coupling strengths.

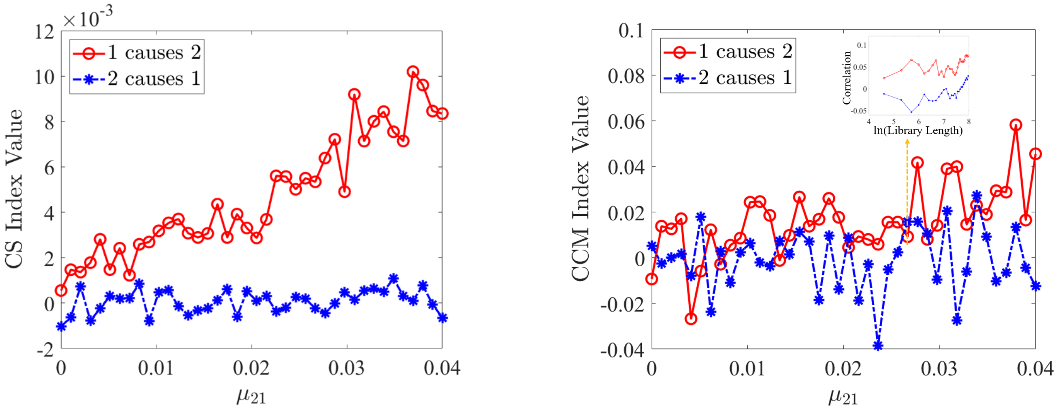

(a) (b)

FIG. S14. Comparison of causation detection with continuity scaling and CCM for the unidirectionally nonlinearly coupled Hénon system (S3.7). For CCM, the embedding dimension and delay time are 5ω and 1ω respectively and the length of library time series varies from 100 to 2900. Notice that CCM has reversed wrong identifications for some coupling strengths (see the subpanel for the corresponding converging curves [2]).

D. Inferring networks of causal interactions

We test the power of our continuity scaling framework in inferring networks of causal interactions from multivariate time series. Here the pairwise inference is considered while generalization of the CS framework to multivariate version will be included in our future work. To be concrete, each network has 5 nodes (i.e., $N_v = 5$) that interact with each other according to the chain, ring, or tree topology, as shown in Figs. S15(a)-15(c).

Discrete time nodal dynamics. We consider the case where the nodal dynamical system is the ecological model (S3.1). For convenience, we rewrite the system equation here:

$$x_{i,t+1} = x_{i,t}\left(r_i - r_i x_{i,t} - \sum_{j\neq i}\mu_{ij}x_{j,t}\right),$$

where $i = 1, \ldots, N_V$, $t \in \mathbb{N}$. The observational functions are $u_i(x_i) = x_i$, the embedding parameters are $d_i = 5$ and $\tau_i = 1$ for $i = 1, \cdots, 5$, and other parameters are $N_\varepsilon = 33$, $e = 0.001$, and $E = 0$. For each network topology, the parameters and the coupling strengths in model (S3.1) are set as follows:

- *Chain topology:* $r_1 = 3.75$, $r_2 = 3.78$, $r_3 = 3.76$, $r_4 = 3.8$, $r_5 = 3.76$, and $\mu_{i+1,i} = 0.07$ for $i = 1, 2, 3, 4$, and all other coupling strengths are 0.
- *Ring topology:* $r_1 = 3.8$, $r_2 = 3.77$, $r_3 = 3.78$, $r_4 = 3.79$, $r_5 = 3.78$, and $\mu_{(i+1)\,\mathrm{mod}\,5,i} = 0.07$ for $i = 1, 2, 3, 4, 5$ with other coupling parameters being 0.
- *Tree topology:* $r_1 = 3.8$, $r_2 = 3.78$, $r_3 = 3.76$, $r_4 = 3.77$, $r_5 = 3.74$, and $\mu_{i+1,i} = \mu_{i+3,i} = 0.07$ for $i = 1, 2$ with other coupling parameters being 0.

For all the cases, the calculated values of the slope $s_{\boldsymbol{u}_i \hookrightarrow \boldsymbol{u}_j}$ characterizing the causation from x_i to x_j are displayed in Fig. S15(d) and in Figs. 3(c) and 3(d) in the main text. To further characterize the performance of our continuity scaling framework for causal network inferences, we plot the Receiver Operating Characteristics (ROC) curves and calculate the corresponding areas under the ROC curves (AUROCs). As shown in Fig. S15(e), all the AUROC values approach one, demonstrating the superior power of our framework in identifying and quantifying causal interactions in networks.

Continuous time nodal dynamics. We study networks whose nodal dynamics are those of the Lorenz system (S3.3). We also rewrite the system equation here:

$$\begin{aligned} \dot{x}_{i,t} &= \sigma_i(y_{i,t} - x_{i,t}) + \textstyle\sum_{j\neq i} \mu_{ij} x_{j,t}, \\ \dot{y}_{i,t} &= x_{i,t}(\rho_i - z_{i,t}) - y_{i,t}, \\ \dot{z}_{i,t} &= x_{i,t} y_{i,t} - \beta_i z_{i,t}, \end{aligned}$$

where $i = 1, \ldots, N_V,\ t \in \mathbb{R}$. The parameters for the five nodes are taken as: $(\sigma_1, \rho_1, \beta_1) = (10.01, 27.972, 2.668)$, $(\sigma_2, \rho_2, \beta_2) = (9.99, 28.028, 2.6672)$, $(\sigma_3, \rho_3, \beta_3) = (10.012, 27.944, 2.6656)$, $(\sigma_4, \rho_4, \beta_4) = (9.98, 27.9608, 2.66934)$, and $(\sigma_5, \rho_5, \beta_5) = (10.04, 28.056, 2.664)$. The embedding parameters are $d_i = 7$ and $\tau_i = 2\omega$ for $i = 1, \cdots, 5$. The sampling duration is $\omega = 0.016$. Other parameter values are $N_\varepsilon = 33$, $e = 0.001$, and $E = 8$. For each network topology, the coupling parameters and the observational functions are as follows:

- *Chain topology:* $\mu_{i+1,i} = 3$ for $i = 1, \cdots, 4$ with the other coupling strengths being 0, and the observational functions are $u_i(x_i, y_i, z_i) = y_i$ for $i = 1, \cdots, 5$.
- *Ring topology:* $\mu_{(i+1) \bmod 5, i} = 3$ for $i = 1, \cdots, 5$ with all other coupling strengths being 0, and the observational functions are $u_i(x_i, y_i, z_i) = x_i - 0.2\cos(y_i) y_i + 2\sin(z_i)$ for $i = 1, \cdots, 5$.
- *Tree topology:* $\mu_{i+1,i} = \mu_{i+3,i} = 3$ for $i = 1, 2$ with the other coupling strengths being 0, and the observational functions are $u_i(x_i, y_i, z_i) = y_i$ for $i = 1, \cdots, 5$.

In all cases, the values of the slope $s_{\boldsymbol{u}_i \hookrightarrow \boldsymbol{u}_j}$ characterizing the causal interaction from (x_i, y_i, z_i) to (x_j, y_j, z_j) are shown in Figs. S16(a)-16(c). The statistical ROC curves with their AUROCs are displayed in Fig. S16(d), validating the accuracies of the inferred causal interactions in the networks.

E. Test of real-world datasets

1. *Synthetic gene regulatory networks*

This real-world example has been described in the main text. Here we provide necessary additional information on the dataset and important numerical simulation parameters. We consider five different networks consisting of 20 genes, which are randomly selected from five 100-genes-networks for each. One of the network structures is presented in Fig. 5(a) of the main text and the other four structures are shown in Fig. S17. Available are time series of 10 realizations (21 points each) of gene's expressions, which are combined as one of 210 points for each gene in the phase space reconstruction procedure. The

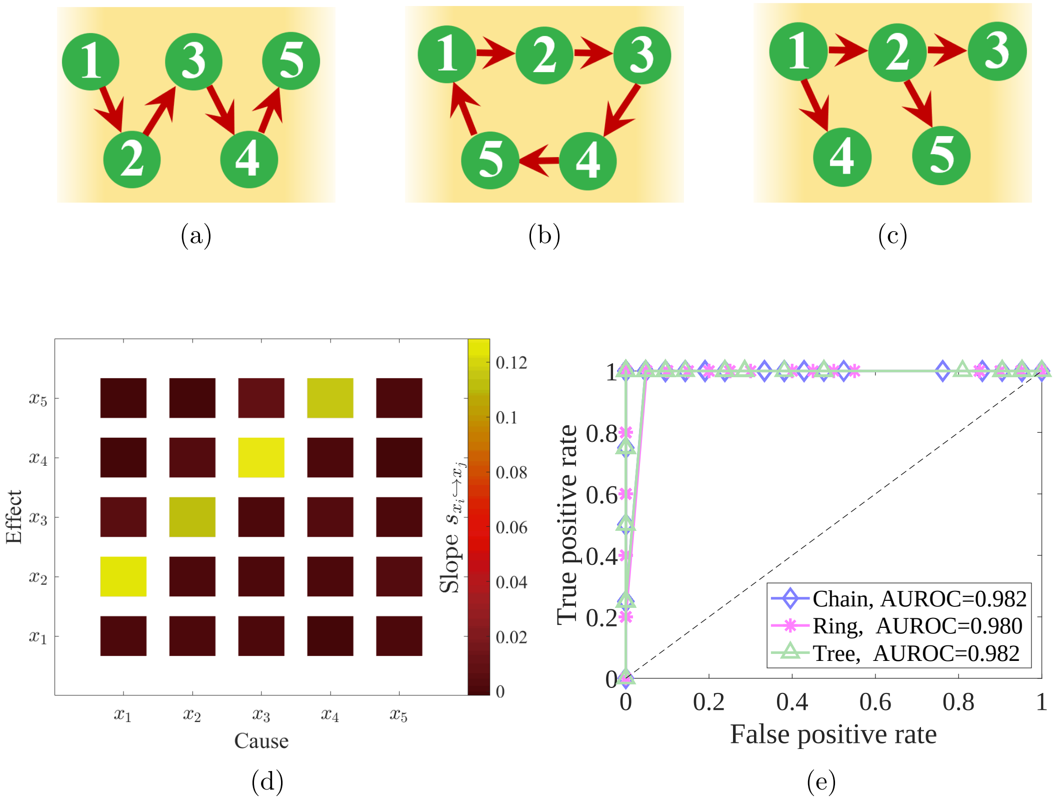

(a) (b) (c)

(d) (e)

FIG. S15. Inferring causal interactions in networks with the continuity scaling framework. The nodal dynamics are governed by the coupled ecological model of five species. The network structures are (a) chain, (b) ring, and (c) tree. For each case, the results of inferred causation are presented in (d) (chain) as well as in Figs. 3(c) (ring) and 3(d) (tree) of the main text. (e) The corresponding ROC curves and their AUROC values representing high detection accuracies.

embedding dimension and delay time are 2 and 1 respectively. Applying our continuity scaling framework to the time series we obtain the corresponding ROC curves with their AUROC values shown in Fig. 5(b) of the main text.

2. Fishery landings and sea surface temperature data

The California landings data for Pacific sardine and northern anchovy and the sea surface temperature (SST) data are acquired and pre-processed following the supplementary materials of [2].

In each run of continuity scaling, the embedding dimension is 3 and embedding lag is 1 and other parameters are $N_\varepsilon = 33$, $e = 0.001$ and $E = 0$. Each p-value is calculated with 250 random surrogates. Detailed continuity scaling indexes and their p-values are listed in Tab. S12.

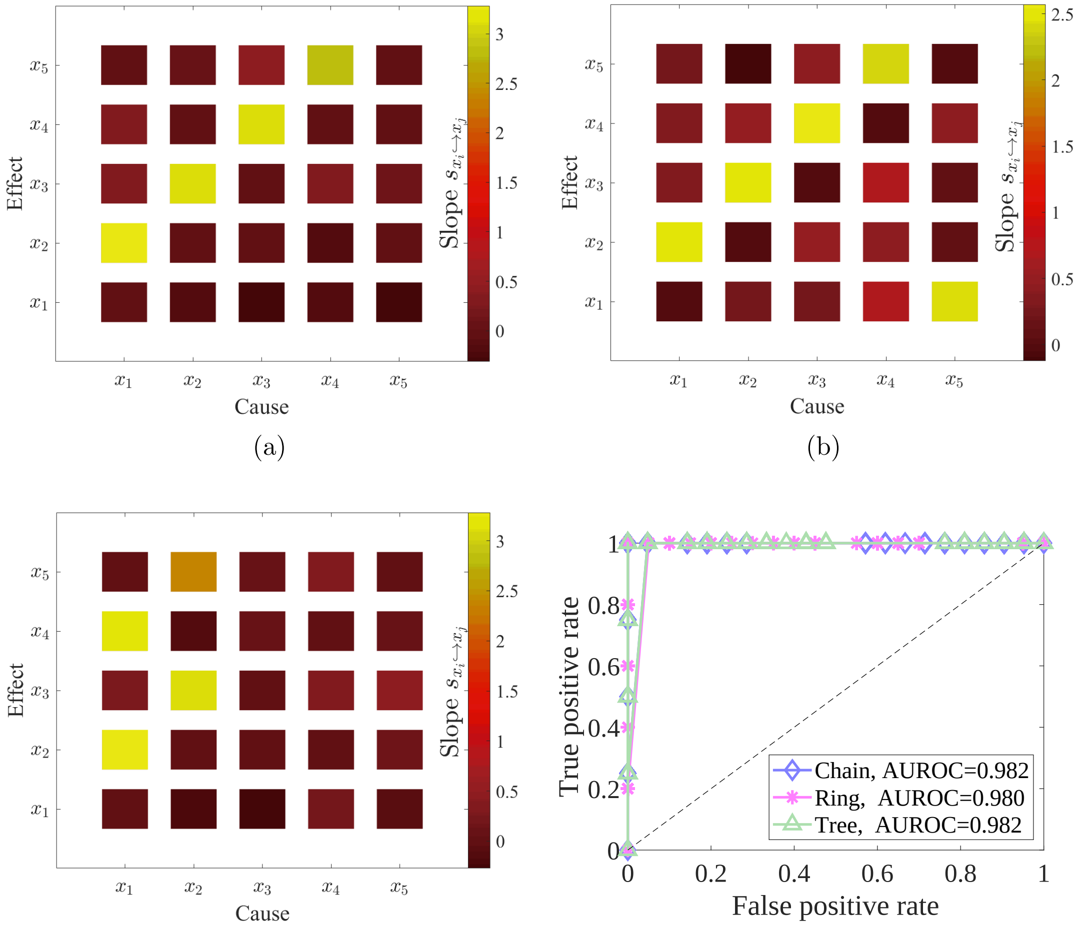

(a) (b)

(c) (d)

FIG. S16. Inferring causal interactions in networks with continuous time nodal dynamics. The nodal dynamics are described by the Lorenz system (S3.3). The network structures are chain, ring, and tree as in Figs. S15(a)-15(c). The results of causal inference for the three network structures are shown in (a-c), respectively. (d) The corresponding ROC curves and their AUROC values.

3. *World COVID-19 pandemic daily cases*

We analyze the COVID-19 pandemic data of 19 representitave countries. Time series of daily cumulative confirmed COVID-19 cases from January 22nd 2020 to February 15th 2021 for each country is downloaded from https://datahub.io/core/covid-19#data, and then first-differenced to obtain the time series of daily new confirmed COVID-19 cases. Few negative data points are due to data corruption and are set as zero. Seven-day moving average is applied to the daily new cases time series.

As shown in Fig. S18(a) the pandemic situation in China experiences a remarkable change: severe at first and under control afterwards, and the critical day 100 is suitable to divide these two stages (see below). Thus we split the times series into two segments: day 1 to day 100 (Stage 1) and day 101 to day 391 (Stage 2), and compare the causal effect from China to other countries at these stages. Causation is confirmed pairwisely if the p-value of its continuity scaling index is less than 0.05. The embedding parameters

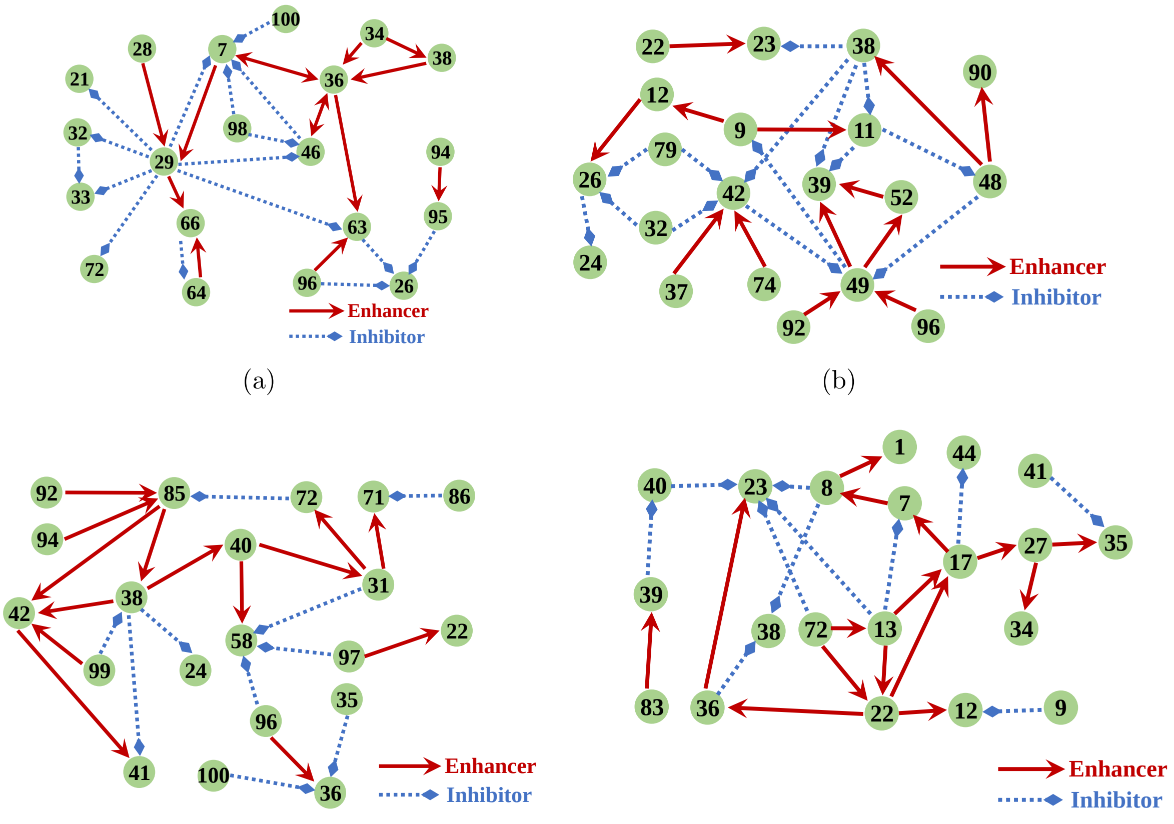

(a) (b)

(c) (d)

FIG. S17. The four networks together with Fig. 5(a) of the main text, with which our continuity scaling framework is tested.

TABLE S12. Inferring causal interaction among SST and landings data for Pacific sardine and northern anchovy. Slopes of the regression lines of the scaling relations and their p-values are listed.

	slope	p-value ($< \mathbf{0.05}$)
$s_{\text{SST}\hookrightarrow\text{Sardine}}$	**0.0435**	**0.0000**
$s_{\text{Sardine}\hookrightarrow\text{SST}}$	-0.0012	0.6943
$s_{\text{SST}\hookrightarrow\text{Anchovy}}$	**0.0462**	**0.0001**
$s_{\text{Anchovy}\hookrightarrow\text{SST}}$	-0.0239	0.9837
$s_{\text{Sardine}\hookrightarrow\text{Anchovy}}$	0.0025	0.3411
$s_{\text{Anchovy}\hookrightarrow\text{Sardine}}$	**0.0105**	**0.0237**

are $d = 3$ and $\tau = 1$, and other parameters are $N_\varepsilon = 33$, $e = 0.001$ and $E = 0$ for each run. Each p-value is calculated with 200 random surrogates. The detected pairwise causal links are presented in Figs. S18(c)-S18(d) for two stages respectively. Particularly, the detected causal links from China to other countries are depicted in Fig. 7 of the main text. Abbreviation (from ISO 3166 country codes, https://www.iso.org/iso-3166-country-codes.html) or index number denoting each country is listed in Tab. S13.

Additionally, we show that critical day, the last day of Stage 1, can be chosen with moderate freedom and this won't harm the soundness of our result. We split the daily

TABLE S13. Abbreviation and index number used in Fig. 7 of the main text, Fig. S18 and Tab. S14 for each country are listed here.

No.	Abbr.	Country
1	CHN	The People's Republic of China
2	GBR	The United Kingdom of Great Britain and Northern Ireland
3	AUS	The Commonwealth of Australia
4	FRA	The French Republic
5	DEU	The Federal Republic of Germany
6	ITA	The Italian Republic
7	JPN	Japan
8	MYS	Malaysia
9	MEX	The United Mexican States
10	SGP	The Republic of Singapore
11	ZAF	The Republic of South Africa
12	ESP	The Kingdom of Spain
13	SWE	The Kingdom of Sweden
14	CHE	The Swiss Confederation
15	USA	The United States of America
16	KOR	The Republic of Korea
17	BEL	The Kingdom of Belgium
18	NLD	The Kingdom of the Netherlands
19	GRC	The Hellenic Republic

confirmed cases time series of all contries by day D ranging from 94 to 106, and conduct analogous analysis to detect causal links. A directional links labelled by "1" with causation or "0" without causation. We compare the results between critical day D and 100 by counting discrepant results among all links and calculated the proportion. As shown in Fig. S18(b), for all Ds, the proportion of variated results does not exceed 5%, and particularly, the conclusion that no country is under the influence of China at Stage 2 always holds.

For CCM, the embedding dimension is 3 and embedding lag is 1. At the two stages, we use 44, 128 points as library respectively, and calculate CCM index with 30, 90 length time series respectively [2]. Emperical threshold is selected where the largest 1/3 links are identified as positive detections (see [2, 3] for more information on the issues of threshold selection).

The prevalence of COVID-19 pandemic in China exists only at Stage 1, while daily cases at Stage 2 are fewer as shown in Fig. 7 of the main text which are mainly imported cases as reported by the goverment (http://en.nhc.gov.cn/DailyBriefing.html). Therefore minor causal influence from China to other countries can be supposed at Stage 2. However as shown in Tab. S14, at Stage 2 CCM detects a remarkable number of countries still under the influence of China and produces results hard to interpret, lowering its reliablity in widely use.

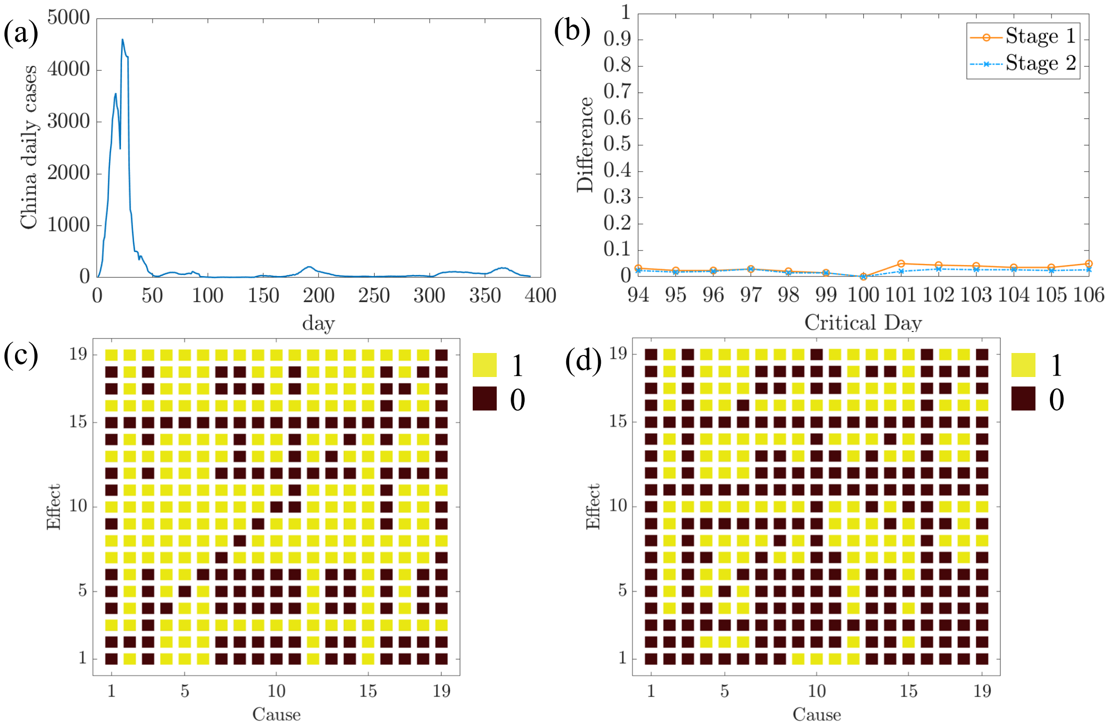

FIG. S18. The 7-day moving averaged daily cases time series of China is plotted in (a). The pairwise causal links detected by continuity scaling from COVID-19 pandemic times series at both stages are illustrated in (c, d). A directional link is colored yellow with causation ("1") or brown without causation ("0"). Each country is represented by its index number listed in Tab. S13. The results of Stage 1 and 2 are presented in (c) and (d) respectively. For critical day, the last day of Stage 1, D ranging from 94 to 106, the proportion of changed causal links compared with critical day 100 is plotted in (b).

TABLE S14. Countries under the influence of China detected by CCM at both stages.

Stage	Countries
1	FRA, DEU, ITA, MYS, ESP, CHE, BEL, NLD
2	GBR, MYS, MEX, ZAF, USA

4. Air pollutants and hospital admission records from Hong Kong

The dataset contains the records of daily air pollutants and of the daily admissions of cardiovascular (Cardio.) disease and respiratory (Resp.) diseases in major hospitals of Hong Kong, China [4, 5] from 1997 to 1999. Every time series contains 1032 points, one for each day. The causal influences of four pollutants, i.e., NO_2, O_3, respirable suspended particulates (Rspar.), and SO_2, on the hospital admissions of Cardio. and Resp. diseases are tested. For all the time series, the embedding dimension and delay time are $d = 4$ and $\tau = 1$, and other parameter values are $N_\varepsilon = 33$, $e = 0.001$, and $E = 0$. The estimated values of the slope $s_{\text{Pollutant}\hookrightarrow\text{Disease}}$ and their p-values are listed in Tab. S15. It can be seen that the instantaneous influences of NO_2 on both Cardio. and Resp. diseases are relatively strong. In addition, the instantaneous impact of O_3 on Cardio. disease and that

TABLE S15. Causal influences, quantified by values of the slope $s_{\text{Pollutant}\hookrightarrow\text{Disease}}$, of four pollutants on the hospital admissions of Cardio. and Resp. diseases, where 300 surrogates are used to test the statistical significance.

	$s_{\text{Pollutant}\hookrightarrow\text{Disease}}$		p-value ($<$ **0.05**)	
Pollutant	Cardio.	Resp.	Cardio.	Resp.
NO_2	**0.5722**	**0.4139**	**0.0000**	**0.0276**
O_3	**0.2427**	0.0856	**0.0000**	0.6529
Rspar.	0.0002	0.0151	0.8404	0.8239
SO_2	-0.0716	**0.1077**	1.0000	**0.0000**

of SO_2 on Resp. disease are also significant, which are highly consistent with previous results [6, 7].

IV. COMPARISONS WITH TYPICAL CROSS-MAP-BASED METHODS

A cross map is defined originally based on the strict correspondence of the time index between the reconstructed manifolds, which is not directly relevant to the existing causal relation, leading to the long-standing question of the use of the information about the effect variable to estimate that of the causal variable. Ref. [8] provides a conceptual explanation from the viewpoint of information flow, which still calls for a rigorous demonstration from the mathematical viewpoint. The definition and the arguments presented in the main text not only provide a resolution to this puzzle in the estimation order but, more significantly, establish a rigorous framework to ascertain reliably and quantify accurately the causal interactions.

We analyze the deficiencies of representative existing cross-map-based methods for causality detection and carry out a comparison study based on benchmark models with known ground truth to demonstrate that our continuity scaling framework is able to overcome the difficulties.

A. Comparison with topological causality

A recently developed technique is based on the concept of topological causality [9]. Let $\boldsymbol{F}$ be a dynamical system on a compact manifold $\mathcal{M}$ with two observational functions: ϕ and ψ, which are smooth functions from $\mathcal{M}$ to $\mathbb{R}$. Suppose further that

$$\begin{aligned}\boldsymbol{\Phi}(\boldsymbol{x}) &= (\phi(\boldsymbol{x}), \phi(\boldsymbol{F}^{\tau}(\boldsymbol{x})), \cdots, \phi(\boldsymbol{F}^{(d-1)\tau}(\boldsymbol{x}))) : \mathcal{M} \to \mathcal{M}_{\phi} = \Phi(\mathcal{M}) \subset \mathbb{R}^{d},\\ \boldsymbol{\Psi}(\boldsymbol{x}) &= (\psi(\boldsymbol{x}), \psi(\boldsymbol{F}^{\tau}(\boldsymbol{x})), \cdots, \psi(\boldsymbol{F}^{(d-1)\tau}(\boldsymbol{x}))) : \mathcal{M} \to \mathcal{M}_{\psi} = \Psi(\mathcal{M}) \subset \mathbb{R}^{d}\end{aligned}$$

are embedding and thus are diffeomorphism to image. Let $\boldsymbol{\phi}_t = (\phi(\boldsymbol{x}_t), \ldots, \phi(\boldsymbol{F}^{(d-1)\tau}(\boldsymbol{x}_t)))$ and $\boldsymbol{\psi}_t = (\psi(\boldsymbol{x}_t), \ldots, \psi(\boldsymbol{F}^{(d-1)\tau}(\boldsymbol{x}_t)))$, where $\boldsymbol{x}_{t+1} = \boldsymbol{F}(\boldsymbol{x}_t)$. Define a cross mapping $\Gamma_{\phi\psi}$: $\mathcal{M}_{\phi} \to \mathcal{M}_{\psi}$ through the correspondence from $\boldsymbol{\phi}_t$ to $\boldsymbol{\psi}_t$ based on the time index t, and further define the extension measure $e^{t}_{\phi\psi}$ by the product of the singular, larger than one values of the Jacobian matrix of $\Gamma_{\phi\psi}$ evaluated at $\boldsymbol{\phi}_t$. The local topological causality from ψ_t to ϕ_t is defined as $C^{t}_{\psi\to\phi} = (1 + \ln e^{t}_{\phi\psi})^{-1}$, and the topological causality from ψ to ϕ

is defined as $C_{\psi\to\phi} = (1 + \langle \ln e^t_{\phi\psi} \rangle_t)^{-1}$, in which $\langle \ln e^t_{\phi\psi} \rangle_t$ represents an average of $\ln e^t_{\phi\psi}$ over all time index t.

We wish to point out that the definition of topological causality is mathematically incomplete and thus cannot resolve the long-standing question of using information about the effect variables to infer that of the causal variables. In particular, eliminating the singular values less than one in its definition is likely to lead to inaccurate evaluation of causality, and the coupling strength may not consistently correspond to the strength of the detected causal interaction. This can be demonstrated through the following continuous time linear dynamical system:

$$\dot{x} = x - \mu y, \quad \dot{y} = y,$$

where μ is the coupling parameter. For simplicity, it is possible to consider topological causality in a local region of the phase space (e.g., a neighborhood of the point $(2, 1)$), since local topological causality index is only evaluated at the investigated point. We consider typical cases here, for example, μ ranging in $[0, 1]$ and (x, y) near $(2, 1)$. Therefore, a one-dimensional system is considered as follows. We localize the phase space by multiplying a real-valued smooth function $\xi : \mathbb{R}^2 \to \mathbb{R}$ ranging in $[0, 1]$ at the right-hand side of the original equations, with ξ supported in an open neighborhood of $(x, y) = (2, 1)$ contained in $\{\, (x, y) \,|\, x > y > 0 \,\}$ and $\xi(2, 1) = 1$. The investigated phase space is given by

$$\begin{aligned} L_\mu = \{\, & (x, y) = (\alpha(t), \beta(t)) \,|\, (\alpha(t), \beta(t)) \text{ is a solution of} \\ & \dot{\alpha}(t) = \xi(\alpha, \beta)(\alpha - \mu\beta),\ \dot{\beta}(t) = \xi(\alpha, \beta)\beta,\ \alpha(0) = 2, \beta(0) = 1 \,\}. \end{aligned}$$

In such a one-dimensional phase space, $\dot{x} = \xi(x, y)(x - \mu y)$, $\dot{y} = \xi(x, y)y$ well defines a dynamical system in it. Because of the localization, coordinate projections of the orbit can indeed reconstruct this system by noting that $\xi(x, y)(x - \mu y) \neq 0$, $\xi(x, y)y \neq 0$ on L_μ, and thus maintain the topological characteristics of the original one-dimensional system: $\dot{x} = x - \mu y$, $\dot{y} = y$.

Considering the new system $\dot{x} = \xi(x - \mu y)$, $\dot{y} = \xi y$ on phase space L_μ. Set the observational functions as x and y, let Γ_{xy} be a cross mapping as the correspondence from $\mathcal{M}_x$ to $\mathcal{M}_y$ based on the time index, and denote as M^t_{xy} the Jacobian matrix of Γ_{xy} at time t. Analytically, we have

$$M^t_{xy} = \frac{\mathrm{d}y}{\mathrm{d}x} = \frac{1}{x/y - \mu}.$$

As defined, e^t_{xy} is the singular value of M^t_{xy} which is larger than one. Typically, for $x,\ y > 0$, if the coupling parameter μ increases from 0 to x/y, M^t_{xy} increases from y/x to $+\infty$, and e^t_{xy} increases from $\max\{1, y/x\}$ to $+\infty$. Consequently, the measure of the topological causality, $C^t_{y\to x} = (1 + \ln e^t_{xy})^{-1}$, decreases monotonously from $(1 + \ln \max\{1, y/x\})^{-1}$ to 0. That is, a larger value of the coupling parameter does not imply a more significant causation detected - a result that is not consistent with the dynamical behavior of the system.

We compare the performance of our continuity scaling framework with topological causality using the algorithms according to the original TC measuring by the index $C_{\psi\to\phi}$. We first consider time series generated by the unidirectionally coupled ecological model (S3.1) with $N_V = 2$, $(r_1, r_2) = (3.8, 3.7)$, $\mu_{12} = 0$, and μ_{21} changing its value from 0 to 0.05. As shown in Fig. S21, our continuity scaling framework works well in detecting causation for all values of μ_{21}, while the topological causality method fails for small values of μ_{21}.

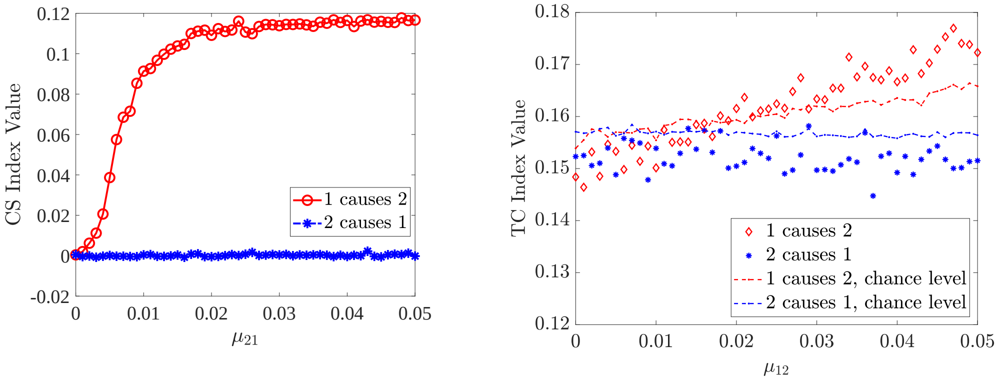

(a) (b)

FIG. S19. Results of comparison study using data from the unidirectionally coupled ecological model (S3.1) of two species: $x_1 \hookrightarrow x_2$. (a) Results from our continuity scaling framework with $N_\varepsilon = 33$, $e = 0.001$, and $E = 0$. (b) Results from the topological causality method, where the number of points in the neighborhood is taken to be $k = 15$. For all cases, the observational functions are $u_i(x_i) = x_i$ and the embedding parameters are $d_i = 3$ and $\tau_i = 1$ for $i = 1, 2$.

The second example is the unidirectionally coupled Bernoulli oscillators:

$$\begin{aligned} x_{1,t+1} &= (1.9 \cdot x_{1,t} - \mu_{12} \cdot x_{2,t}) \bmod 1, \\ x_{2,t+1} &= (2.3 \cdot x_{2,t}) \bmod 1, \end{aligned} \tag{S4.1}$$

where the coupling parameter μ_{12} changes its value systematically from 0 to 0.02. Figure S22 presents the results of the comparison study, demonstrating the superior accuracy of our continuity scaling framework for detecting and quantifying causation. The topological causality method reveals completely wrong causation in the weakly coupling regime of small μ_{12} values and exhibits a reversed relation with the increase of μ_{12}.

B. Comparison with convergent cross mapping

We also carry out a comparison study with CCM method based on benchmark models with known ground truth [2]. We calculate the slope values estimated from the linear regression of the convergence curve with increasing length of the library time series in CCM.

We first consider time series generated by the unidirectionally coupled ecological model (S3.1) with $N_V = 2$, $(r_1, r_2) = (3.8, 3.7)$, $\mu_{12} = 0$, and μ_{21} changing its value from 0 to 0.05. As shown in Fig. S21, both our continuity scaling framework and CCM work well in detecting causation for all values of μ_{21}. However, the CCM measure exhibits an increasing level of fluctuations as the coupling parameter is increased.

The second example is the unidirectionally coupled Bernoulli maps:

$$\begin{aligned} x_{1,t+1} &= (1.9 \cdot x_{1,t} - \mu_{12} \cdot x_{2,t}) \bmod 1, \\ x_{2,t+1} &= (2.3 \cdot x_{2,t}) \bmod 1, \end{aligned} \tag{S4.2}$$

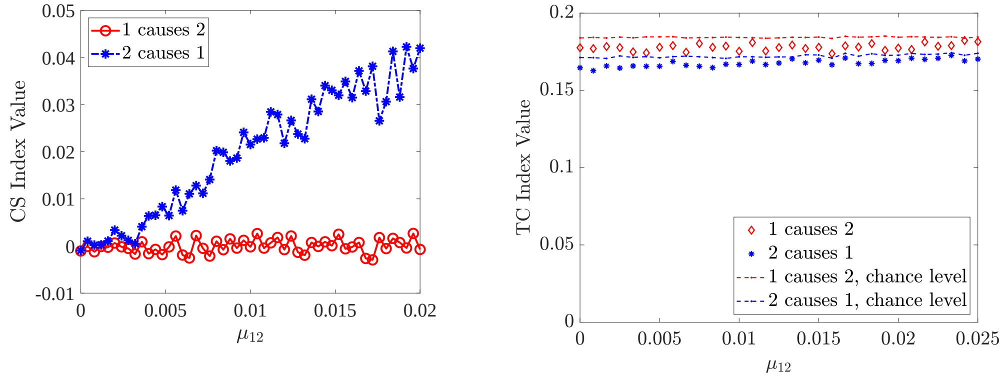

(a) (b)

FIG. S20. Results of comparison study using data from the unidirectionally coupled Bernoulli oscillators (S4.2): $x_2 \hookrightarrow x_1$. (a) Results from our continuity scaling framework. (b) Results from the topological causality method. The embedding parameters are $d_i = 4$ and $\tau_i = 1$ for $i = 1, 2$, and the observational functions and other parameter values are the same as those in Fig. S21.

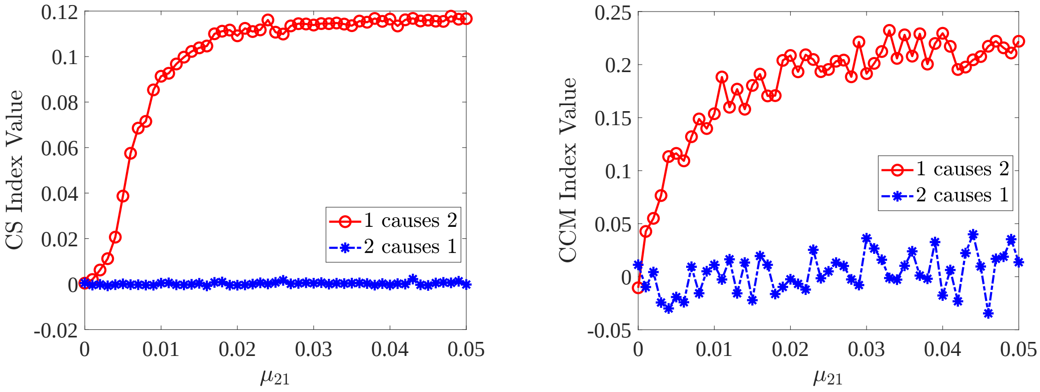

(a) (b)

FIG. S21. Results of comparison study using data from the unidirectionally coupled ecological model (S3.1) of two species: $x_1 \hookrightarrow x_2$. (a) Results from our continuity scaling framework with $N_\varepsilon = 33$, $e = 0.001$, and $E = 0$. (b) Results from the CCM method. For all cases, the observational functions are $u_i(x_i) = x_i$ and the embedding parameters are $d_i = 3$ and $\tau_i = 1$ for $i = 1, 2$.

where the coupling parameter μ_{12} changes its value systematically from 0 to 0.02. Figure S22 presents the results of the comparison study, demonstrating the superior accuracy of our continuity scaling framework for detecting and quantifying causation. The CCM method fails for most values of the coupling parameter. The reason for the failure lies in that the Bernoulli maps have uniformly expanding properties with all positive Lyapunov exponents, leading to the sensitivity of detection on the pre-selected radius of the neighborhoods. Increasing the time series length in the CCM method does not provide a resolution. In contrast, the continuity scaling between the dynamically contracting neighborhoods is key to determining the accuracy of causation detection.

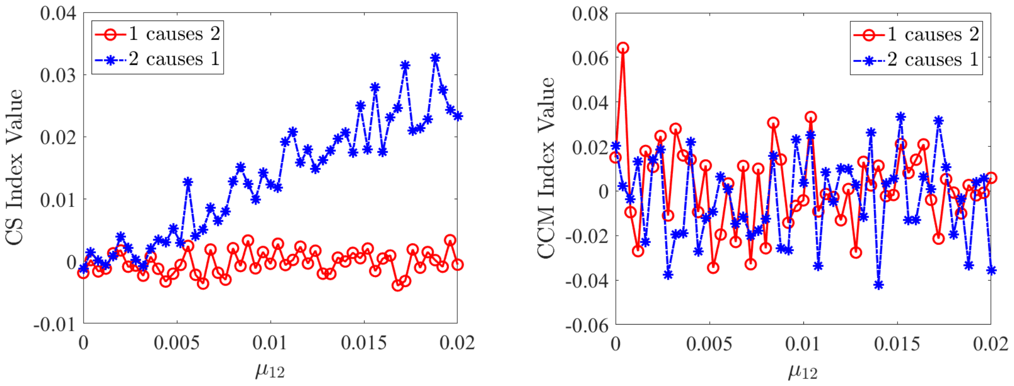

(a) (b)

FIG. S22. Results of comparison study using data from the unidirectionally coupled Bernoulli maps (S4.2): $x_2 \hookrightarrow x_1$. (a) Results from our continuity scaling framework. (b) Results from the CCM method. The embedding parameters are $d_i = 5$ and $\tau_i = 1$ for $i = 1, 2$, and the observational functions and other parameter values are the same as those in Fig. S21.

Though greatly inspired by the cross-map-based methods, we still summarize the essential differences between our CS framework and the cross-map-based methods here. While the correspondence techniques using the time indexes in the traditional cross-map-based methods and our CS framework are almost the same, they differ in one-step time index and also in using a [DD] condition. These differences follow from the consideration and quantification of continuity for different maps (Φ or f). These differences also yield the above example where our framework outperforms the CCM method even using sufficiently large embedding dimensions. Precisely, in the traditional cross-map-based techniques, function properties including continuity regarding the cross-map $Y_t = \Phi(X_t)$ (when Y drives X) are fully and systematically investigated. Thus, correspondence technique using the simultaneous points is taken into account. But we consider the causality using the original dynamical systems, not the cross-map Φ. Particularly, when turning eyes from the cross-map to the original iteration/flow, i.e., $x_{t+1} = f(x_t, y_t)$, correspondence between y_t and x_{t+1} is considered, with one-step time difference naturally arising. This minor difference in implementation in fact is induced by essential difference in changing object of study. Secondly, the above consideration requires the key Condition [DD], which is only needed when considering the original iteration/flow and whose universality is demonstrated in section II. Thirdly, the idea of the CS framework is that causality is reflected in the continuity scaling relationship of the original iteration/flow, i.e., in the scaling relation between changing sizes of the $\varepsilon_{x_{t+1}}$ and δ_{y_t} neighborhoods, which leads to the failure of the CCM method using pre-selected/fixed radius of the neighborhoods in the example of coupled Bernoulli maps, with uniformly expanding properties. These points illustrate the importance of directly investigating the continuity of the original iteration/flow f rather than the cross-map Φ.

In addition, our proposed CS framework has different object of study with all the existing methods and holds essentially different theoretical basis. In fact, the existing causation detection methods, referred to in the main text, can be roughly classified into the following categories: Granger causality based methods, entropy based methods, and cross-map-based methods. While a complete summarization study of the Granger causality based methods and entropy based methods can be referred to many literatures [3, 10], the above comparisons with typical cross-map-based method demonstrate their differences with our CS framework.

---

[1] Eckmann, J.-P. & Ruelle, D. Ergodic theory of chaos and strange attractors. *Reviews of Modern Physics* **57**, 617–656 (1985). doi: 10.1103/RevModPhys.57.617.

[2] Sugihara, G. *et al.* Detecting causality in complex ecosystems. *Science* **338**, 496–500 (2012). doi: 10.1126/science.1227079.

[3] Leng, S. *et al.* Partial cross mapping eliminates indirect causal influences. *Nature Communications* **11**, 1–9 (2020). doi: 10.1038/s41467-020-16238-0.

[4] Fan, J., Zhang, W. *et al.* Statistical estimation in varying coefficient models. *Annals of Statistics* **27**, 1491–1518 (1999). doi: 10.1214/aos/1017939139.

[5] Wong, T. W. *et al.* Air pollution and hospital admissions for respiratory and cardiovascular diseases in hong kong. *Occupational and Environmental Medicine* **56**, 679–683 (1999). doi: 10.1103/PhysRevE.96.012221.

[6] Ma, H. *et al.* Detection of time delays and directional interactions based on time series from complex dynamical systems. *Physical Review E* **96**, 012221 (2017).

[7] Milojevic, A. *et al.* Short-term effects of air pollution on a range of cardiovascular events in england and wales: case-crossover analysis of the minap database, hospital admissions and mortality. *Heart* **100**, 1093–1098 (2014). doi: 10.1136/heartjnl-2013-304963.

[8] Paluš, M., Krakovská, A., Jakubík, J. & Chvosteková, M. Causality, dynamical systems and the arrow of time. *Chaos: An Interdisciplinary Journal of Nonlinear Science* **28**, 075307 (2018). doi: 10.1063/1.5019944.

[9] Harnack, D., Laminski, E., Schünemann, M. & Pawelzik, K. R. Topological causality in dynamical systems. *Physical Review Letters* **119**, 098301 (2017). doi: 10.1103/PhysRevLett.119.098301.

[10] Edinburgh, T *et al.* Causality indices for bivariate time series data: A comparative review of performance. *Chaos: An Interdisciplinary Journal of Nonlinear Science* **31**, 083111 (2021). doi: 10.1063/5.0053519.